

Stellar Loci. VII. Photometric Metallicities of 5 Million FGK Stars Based on GALEX GR6+7 AIS and Gaia EDR3

XUE LU ^{1,2} HAIBO YUAN ^{1,2} SHUAI XU ^{1,2} RUOYI ZHANG ^{1,2} KAI XIAO ^{1,2,3} YANG HUANG ³
TIMOTHY C. BEERS ^{4,5} AND JIHYE HONG ^{4,5}

¹*Institute for Frontiers in Astronomy and Astrophysics, Beijing Normal University, Beijing 102206, China*

²*Department of Astronomy, Beijing Normal University No.19, Xijiekouwai St, Haidian District, Beijing, 100875, China*

³*School of Astronomy and Space Science, University of Chinese Academy of Sciences, Beijing 100049, China*

⁴*Department of Physics and Astronomy, University of Notre Dame, Notre Dame, IN 46556, USA*

⁵*Joint Institute for Nuclear Astrophysics – Center for the Evolution of the Elements (JINA-CEE), USA*

(Received XXX; Revised YYY; Accepted ZZZ)

ABSTRACT

We combine photometric data from GALEX GR6+7 AIS and Gaia EDR3 with stellar parameters from the SAGA and PASTEL catalogs to construct high-quality training samples for dwarfs ($0.4 < \text{BP} - \text{RP} < 1.6$) and giants ($0.6 < \text{BP} - \text{RP} < 1.6$). We apply careful reddening corrections using empirical temperature- and extinction-dependent extinction coefficients. Using the two samples, we establish a relationship between stellar loci (NUV–BP vs. BP–RP colors), metallicity, and M_G . For a given BP–RP color, a 1 dex change in $[\text{Fe}/\text{H}]$ corresponds to an approximately 1 magnitude change in NUV–BP color for solar-type stars. These relationships are employed to estimate metallicities based on NUV–BP, BP–RP, and M_G . Thanks to the strong metallicity dependence in the GALEX NUV-band, our models enable a typical photometric-metallicity precision of approximately $\sigma_{[\text{Fe}/\text{H}]} = 0.11$ dex for dwarfs and $\sigma_{[\text{Fe}/\text{H}]} = 0.17$ dex for giants, with an effective metallicity range extending down to $[\text{Fe}/\text{H}] = -3.0$ for dwarfs and $[\text{Fe}/\text{H}] = -4.0$ for giants. We also find that the NUV-band based photometric-metallicity estimate is not as strongly affected by carbon enhancement as previous photometric techniques. With the Gaia and GALEX data, we have estimated metallicities for about 5 million stars across almost the entire sky, including approximately 4.5 million dwarfs and 0.5 million giants. This work demonstrates the potential of the NUV-band for estimating photometric metallicities, and sets the groundwork for utilizing the NUV data from space telescopes such as the upcoming Chinese Space Station Telescope.

Keywords: metallicity; stellar fundamental parameters; astronomy data analysis

1. INTRODUCTION

Metallicity (metal abundance; generally parametrized by $[\text{Fe}/\text{H}]$), is one of the basic stellar parameters, and plays an important role in studying the formation and evolution of not only stars and stellar populations, but also of galaxies such as the Milky Way. Analyzing the stellar metallicity distribution within the Milky Way provides valuable insights into its origin and evolution

through chemical and kinematic studies (e.g., Beers & Christlieb 2005; Matteucci 2021).

There are two main methods to measure stellar metallicity for large samples of stars utilized to date: spectroscopic and photometric. Spectroscopy has long been the primary approach, and significant progress has been made with large-scale spectroscopic surveys over the past two decades. Notable surveys include the Sloan Digital Sky Survey and the Sloan Extension for Galactic Understanding and Evolution (SDSS/SEGUE; York et al. 2000; Yanny et al. 2009; Rockosi et al. 2022), the Radial Velocity Experiment (RAVE; Steinmetz et al. 2006), the Large Sky Area Multi-Object Fiber Spectro-

scopic Telescope (LAMOST; Deng et al. 2012; Liu et al. 2014), the Apache Point Observatory Galactic Evolution Experiment (APOGEE; Majewski et al. 2017), and the GALactic Archaeology with HERMES (GALAH; Buder et al. 2018). Moderate ($R \sim 7,500$)- to high ($R \gtrsim 20,000$)-resolution spectroscopy can achieve high-precision metallicity estimates, typically around or below 0.1 dex, especially in cases of high spectral signal-to-noise ratios. However, there are also disadvantages to spectroscopy. For example, spectroscopic surveys are more time-consuming and require complex data analysis compared to photometric surveys. Consequently, the number of observed sources collected from the aforementioned surveys represents only a tiny fraction of the estimated total number of stars in the Milky Way. The resulting limited samples, coupled with typically complex selection functions for the targets, poses challenges to obtaining a more complete and unbiased set of metallicity estimates for stars in the Milky Way.

Stellar metallicity can also be obtained by analyzing photometric data; original efforts can be traced back to Schwarzschild et al. (1955), but steady progress in this approach has been made over the intervening decades due to improvements in technology and the use of optimized filters. Stellar colors are not a pure function of the effective temperature; other stellar parameters also have an impact, including the stellar metallicity. Though it has a smaller effect on the stellar color than temperature, the metallicity of a star can still be inferred photometrically. The dependence of stellar loci on metallicity is more pronounced in bluer colors, as metallic absorption lines in the optical region are primarily concentrated in the this wavelength range.

A typical procedure for obtaining photometric-metallicity estimates involves several steps. First, cross-matches of photometric catalogs of stars with available spectroscopic-metallicity estimates are performed. Data quality cuts and careful reddening corrections are then applied for the stars in common. Subsequently, various techniques such as metallicity-dependent stellar loci fitting (e.g., Yuan et al. 2015a), principal component analysis (e.g., Casagrande et al. 2019), stellar isochrone fitting (e.g., An & Beers 2020), neural networks (e.g., Whitten et al. 2021; Yang et al. 2022), and others are employed to establish the relationship between stellar colors and metallicities. This relationship is then further validated and tested using other independent sets of data. Finally, the established relationship is applied to all photometric data that satisfy certain conditions, enabling the determination of photometric metallicities for those sources. Furthermore, it is important to recognize

that the relationship between stellar colors and metallicities varies for stars of different luminosity classes.

Among these methods, the stellar loci fitting method stands out as one of the earliest, and has been widely employed (e.g., Ivezić et al. 2008; Yuan et al. 2015a; Starkenburg et al. 2017; Huang et al. 2019, 2021). Ivezić et al. (2008) used the SDSS colors $u-g$ and $g-r$ to provide photometric metallicities for 2 million dwarfs with a precision of 0.15 dex, down to a metallicity limit of $[\text{Fe}/\text{H}] \sim -2.0$. In a later study, Yuan et al. (2015a) investigated the metallicity dependence of the stellar loci from SDSS and their intrinsic widths after considering effect of metallicity and photometric error, by using recalibrated photometric data from SDSS stripe 82 (Yuan et al. 2015c). It was found that a 1 dex decrease in metallicity results in a decrease of about 0.20/0.02 mag in the $u-g/g-r$ colors and increase of about 0.02/0.02 mag in the $r-i/i-z$ colors, respectively. Additionally, Yuan et al. (2015b) estimated photometric metallicities for half a million FGK stars from SDSS stripe 82 with a typical precision of 0.1 dex by simultaneously fitting de-reddened $u-g$, $g-r$, $r-i$, and $i-z$ colors from SDSS to those predicted for metallicity-dependent stellar loci. After that, Zhang et al. (2021) studied metallicity-dependent SDSS stellar color loci for red giant stars, and measured stellar metallicities in Stripe 82 using the same technique, achieving a typical precision of 0.2 dex. Notably, they observed systematic differences between the metallicity-dependent stellar loci of red giants and main-sequence stars.

Huang et al. (2019, 2022, 2023) apply a similar technique to the photometric data of SkyMapper Southern Survey (SMSS; Onken et al. 2019) DR2 and the Stellar Abundances and Galactic Evolution Survey (SAGES; Fan et al. 2023) DR1, whose optimally designed narrow/medium-band u,v filters enabled photometric-metallicity estimates down to $[\text{Fe}/\text{H}] \sim -3.5$ for a total of some 50 million stars.

Broad-band photometry is generally believed to be unsuitable for photometric-metallicity estimation, due to very weak sensitivity to changes in stellar metallicity. However, by combining data from Gaia EDR3 (Brown et al. 2021) and LAMOST DR7 (Luo et al. 2015) and using the stellar loci fitting technique, Xu et al. (2022a) obtained metallicity estimates for about 27 million stars (including over 20 million dwarfs and 6 million giants) with $10 < G < 16$ across almost the entire sky. They found that, for a given $(\text{BP} - \text{RP})$ color, a 1 dex change in $[\text{Fe}/\text{H}]$ results in a 5 mmag change in the $(\text{BP} - G)$ color for solar-type stars. Despite the very weak sensitivity, the exquisite data quality of the Gaia colors, together with careful reddening corrections and color

calibrations, enable a typical precision of approximately $\delta[\text{Fe}/\text{H}] = 0.2$ dex. Utilizing the extensive dataset of photometric metallicities and considering additional criteria, Xu et al. (2022b) compile an updated catalog of the Best and Brightest metal-poor stars. This catalog offers valuable targets for subsequent high-resolution spectroscopic observations.

Based on previous work, bluer and narrower bands are more sensitive to metallicity; the availability of high-precision photometric data is also highly advantageous for accurate and precise estimates of photometric metallicity. However, thus far, the capability of the near-ultraviolet (NUV) band (with a bandwidth on the order of 1000 Å) data for estimation of photometric metallicities has not yet been fully explored. In this study, we aim to develop the utility of NUV data from the Galaxy Evolution Explorer (GALEX; Martin et al. 2005) for this purpose.

The paper is organized as follows. In Sections 2 and 3, we introduce the data and the method used in this work. The results and a discussion are described in Section 4. The final sample is described in Section 5. Section 6 presents a summary.

2. DATA

2.1. GALEX GR6+7 AIS

GALEX was a NASA Explorer Mission, launched on April 28, 2003, with the primary objective of conducting the first space-based sky survey in both the near and far ultraviolet. GALEX surveys include an all-sky imaging survey, and medium and deep imaging surveys covering specific areas, as well as spectroscopic surveys utilizing grism technology. GALEX simultaneously performs sky surveys in two bands through use of a dichroic beam splitter: far-UV (FUV; 1344 – 1786 Å) and near-UV (NUV; 1771 – 2831 Å). The field-of-view of GALEX is 1.28/1.24°, and the spatial resolution is 4.2/5.3'' for the FUV/NUV, respectively (Morrissey et al. 2007). The GALEX GR6+7 AIS database (Bianchi et al. 2014) is a valuable catalog derived from the mission, containing 214,449,551 source measurements.

2.2. Gaia Early Data Release 3

The Gaia Early Data Release 3 (EDR3; Brown et al. 2021) provides unprecedented photometric data with milli-magnitude precision for over one billion stars in the G , G_{BP} and G_{RP} bands¹. It also provides trigonometric parallaxes and proper motions for nearly 1.5 billion sources. This vast and high-quality dataset serves as an

excellent resource for estimating photometric metallicities for an enormous number of stars.

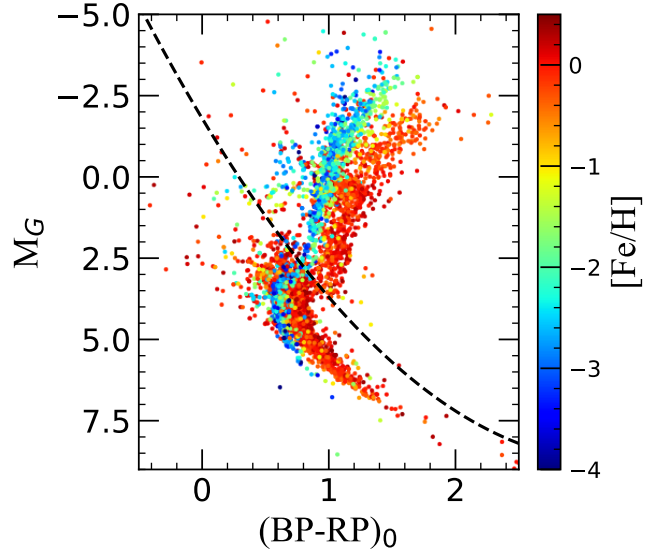


Figure 1. HR diagram of the training samples, color-coded by $[\text{Fe}/\text{H}]$. The dwarfs and giants are separated by the black dashed line (Xu et al. 2022a): $M_G = -(\text{BP} - \text{RP})^2 + 6.5 \times (\text{BP} - \text{RP}) - 1.8$.

2.3. Construction of Training Samples

We obtain spectroscopic data for the training samples by combining metallicity information from the Stellar Abundances for the Galactic Archeology (SAGA; Suda et al. 2008, 2011; Yamada et al. 2013; Suda et al. 2017) and the PASTEL (Soubiran et al. 2010, 2016) catalogs. After removing old and duplicate sources, the number of stars in the combined dataset is 26,350. After performing a cross-match with the GALEX GR6+7 AIS and Gaia EDR3 catalogs, we obtain NUV/BP/RP-band information for 4,026 sources, which are used to construct our final training samples. Considering that the stellar loci in the NUV-band are highly sensitive to metallicity, and the sensitivity differs between giants and dwarfs (Zhang et al. 2021), we divide the selected sources into these two categories using an empirical cut (Xu et al. 2022a), as shown in Figure 1. The cuts for the training samples are as follows:

1. $0.4 < (\text{BP} - \text{RP})_0 < 1.6$ for dwarfs and $0.6 < (\text{BP} - \text{RP})_0 < 1.6$ for giants
2. $-3.5 < [\text{Fe}/\text{H}] < +0.5$ for dwarfs (considering the metallicity dependency is too weak to estimate metallicity for dwarf stars with $[\text{Fe}/\text{H}] < -3.5$ using the GALEX NUV data) and $-5 < [\text{Fe}/\text{H}] < +0.5$ for giants

¹ For simplicity of notation, we refer to the G_{BP} and G_{RP} magnitudes as ‘BP’ and ‘RP’ in the remainder of this paper.

3. $\text{NUV} > 15$ to avoid saturation (Morrissey et al. 2007) and $\text{error}_{\text{NUV}} < 0.1$ to ensure the data quality
4. $E(B - V) < 0.15$. The $E(B - V)$ used here is from the Schlegel et al. (1998, hereafter SFD98) dust reddening map (note that the 14% systematic over-estimated values have been corrected in the empirical reddening coefficients described in Section 3).

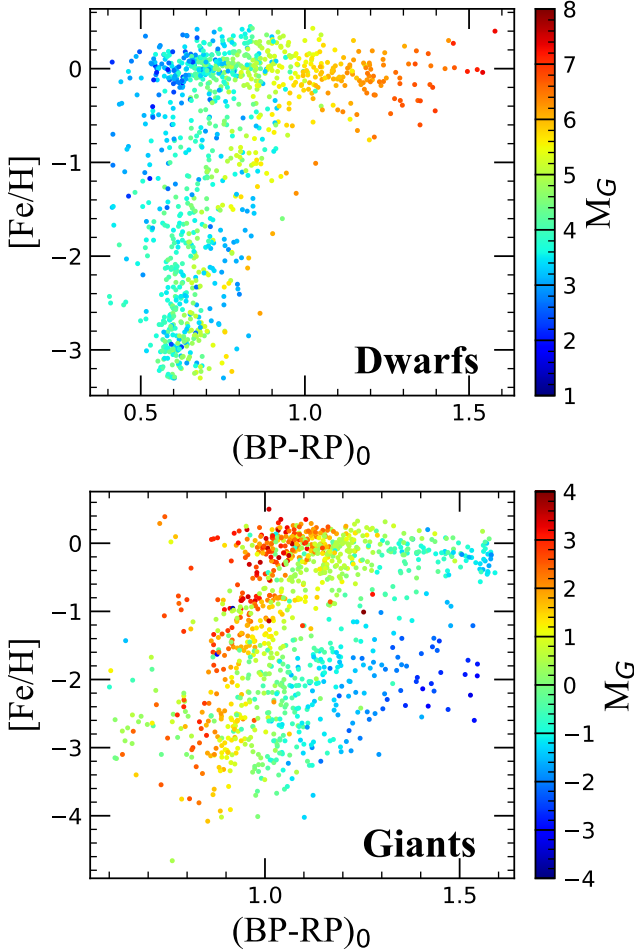


Figure 2. Distributions of the dwarf (top panel) and giant (bottom panel) training samples after cutting in the $[\text{Fe}/\text{H}]$ vs. $(\text{BP} - \text{RP})_0$ plane, color-coded by M_G .

After applying these cuts, the dwarf and giant samples have a very limited number of sources with $-2.5 < [\text{Fe}/\text{H}] < -0.3$. We thus add 200 high-quality dwarfs and giants from LAMOST with $-2.5 < [\text{Fe}/\text{H}] < -0.3$, $\text{SNR}_g(\text{LAMOST}) > 40$, $\text{error}_{\text{NUV}} < 0.05$, $E(B - V) < 0.05$, and $\text{NUV} > 15$ into the dwarf and giant training samples. There are small metallicity offsets between the LAMOST and the previous training samples: -0.07 dex

for dwarfs and -0.06 dex for giants. Finally, a total of 1073 and 1107 sources are selected as our dwarf and giant training samples, respectively. Their distributions in the $[\text{Fe}/\text{H}]$ vs. $(\text{BP} - \text{RP})_0$ plane are shown in Figure 2.

3. METHOD

3.1. Reddening Corrections

Due to the ultra-broad Gaia passbands, it is important to perform careful reddening corrections. Zhang & Yuan (2023) consider the dependence of reddening coefficients on T_{eff} and $E(B - V)$, providing a better description of empirical reddening coefficients than simply single-valued coefficients. According to their results, the reddening coefficients exhibit a stronger dependence on T_{eff} for broader filters (such as the Gaia passbands) and bluer filters (such as the GALEX filters). In this work, we utilize the python package provided by Zhang & Yuan (2023) to obtain T_{eff} - and $E(B - V)$ -dependent reddening coefficients: $R(T_{\text{eff}}, E(B - V))$ for the BP-RP and NUV-BP colors. The intrinsic colors of stars are estimated as follows:

$$\text{color}_0 = \text{color}_{\text{obs}} - R_{\text{color}}(T_{\text{eff}}, E(B - V)) \times E(B - V).$$

All colors referred to hereafter are the intrinsic (de-reddened) colors unless otherwise noted.

In the python package of Zhang & Yuan (2023), the input temperatures could be replaced by BP - RP colors when unavailable, as adopted in this work. During this process, we observe differences in the reddening coefficients between dwarfs and giants. We randomly select 10,000 sources in common with $E(B - V) < 0.5$ from LAMOST DR8 (Luo et al. 2015), Gaia EDR3 and GALEX GR6+7 to present the differences in the BP - RP vs. NUV - BP intrinsic color loci between giants and dwarfs in Figure 3, which illustrates that BP-RP colors differ between dwarfs and giants at the same NUV-BP color. This results in a modest bias in the reddening coefficients obtained from Zhang & Yuan (2023) for giants, mainly due to the lack of giants in their UV sample. Therefore, we make an attempt to correct this bias by subtracting 0.3 mag from BP-RP colors for giants when using the python package of Zhang & Yuan (2023). The result is shown in Figure 4.

3.2. $[\text{Fe}/\text{H}]$ - and M_G -dependent Stellar Loci

Similar to Yuan et al. (2015a), we conduct a polynomial fitting for stellar loci, and employ a minimum χ^2 technique to derive the metallicity for dwarfs and giants, respectively. Unlike Yuan et al. (2015a), we consider the effects of both metallicities and absolute magnitude on stellar loci rather than metallicities alone (see APPENDIX A). A fourth-order three-dimensional

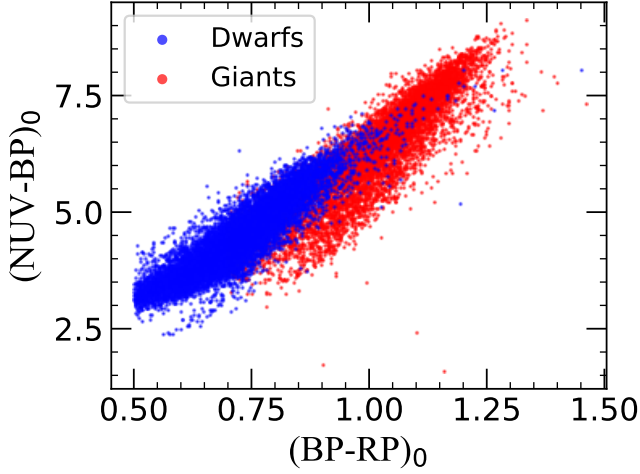


Figure 3. The differences in BP – RP vs. NUV – BP color loci between dwarfs (blue dots) and giants (red dots).

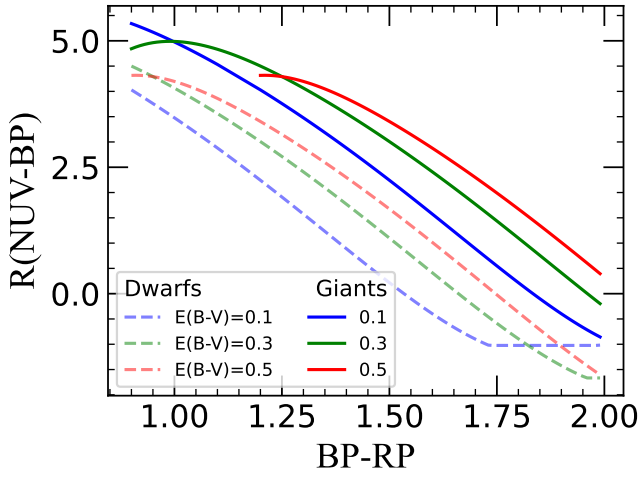


Figure 4. $R_{\text{NUV-BP}}$, as a function of BP–RP, for dwarfs (dashed lines) and giants (solid lines) at different extinction values.

polynomial with thirty-one free parameters is adopted to fit the relationship among NUV–BP, BP–RP color, $[\text{Fe}/\text{H}]$, and M_G for both dwarfs and giants:

$$\begin{aligned}
 (NUV - BP) = & \\
 & p_0 \cdot X^4 + p_1 \cdot Y^4 + p_2 \cdot Z^4 + p_3 \cdot X^3 \cdot Y \\
 & + p_4 \cdot Y^3 \cdot X + p_5 \cdot X^3 \cdot Z + p_6 \cdot Z^3 \cdot X \\
 & + p_7 \cdot Z^3 \cdot Y + p_8 \cdot Y^3 \cdot Z + p_9 \cdot X^2 \cdot Y^2 \\
 & + p_{10} \cdot X^2 \cdot Z^2 + p_{11} \cdot Z^2 \cdot Y^2 + p_{12} \cdot X^3 \\
 & + p_{13} \cdot Y^3 + p_{14} \cdot Z^3 + p_{15} \cdot X^2 \cdot Y + p_{16} \cdot Y^2 \cdot X \\
 & + p_{17} \cdot X^2 \cdot Z + p_{18} \cdot Z^2 \cdot X + p_{19} \cdot Z^2 \cdot Y \\
 & + p_{20} \cdot Y^2 \cdot Z + p_{21} \cdot X^2 + p_{22} \cdot Y^2 + p_{23} \cdot Z^2 \\
 & + p_{24} \cdot X \cdot Y + p_{25} \cdot Y \cdot Z + p_{26} \cdot X \cdot Z \\
 & + p_{27} \cdot X + p_{28} \cdot Y + p_{29} \cdot Z + p_{30}, \quad (1)
 \end{aligned}$$

where X, Y, Z represents the BP–RP color, $[\text{Fe}/\text{H}]$, and M_G , respectively. The M_G here are calculated by:

$$M_G = G - 10 - 5 \times \log_{10} \frac{1}{\text{parallax}} - R_G \times E(B - V),$$

where the parallax values are the Gaia parallaxes corrected by [Lindgren et al. \(2021\)](#), R_G values are from the python package of [Zhang & Yuan \(2023\)](#), and $E(B - V)$ values are from the SFD98 redenning map. During the fitting process, a 3σ -clipping procedure is performed to reject outliers. The fitting coefficients p_i are provided in Table 1.

Table 1. Fitting Coefficients for the Dwarfs and Giants

Coeff.	Giants	Dwarfs
p0	−0.7607	+5.8352
p1	−0.0207	−0.0231
p2	−0.0012	−0.0210
p3	+0.1987	+2.6037
p4	−0.0413	+0.0153
p5	−1.8229	−0.8798
p6	−0.0921	+0.4813
p7	−0.0068	−0.0089
p8	−0.0032	−0.0085
p9	−0.2876	−2.0478
p10	−0.9692	−1.3104
p11	−0.0000	+0.0198
p12	−5.9457	−11.2965
p13	−0.1228	−0.1001
p14	+0.1019	+0.0225
p15	−2.3209	−12.0546
p16	+0.3297	+2.8586
p17	+5.8758	+9.1233
p18	+2.1666	−3.7948
p19	+0.0044	+0.1869
p20	+0.0142	−0.1947
p21	+24.6050	−2.3854
p22	−0.3129	−0.5011
p23	−1.2202	+1.0914
p24	+3.8330	+13.9786
p25	+0.1420	−1.0543
p26	−6.2672	+10.1043
p27	−20.7169	−8.6359
p28	−0.9627	−1.7705
p29	+2.2438	−5.4122
p30	+9.5277	+8.6614

The fitting results for the dwarf training sample are shown in Figure 5. The distribution of the dwarf training sample in the NUV–BP vs. BP–RP plane is plotted in panel (a), color-coded by $[\text{Fe}/\text{H}]$. From inspection, there are clear dividing lines between sources with different metallicities. Panel (b) shows the variations of the stellar locus at $M_G = 4.5$ for different metallicities

relative to the one at $[\text{Fe}/\text{H}] = -0.5$. A 1 dex change in metallicity corresponds to an approximately 1 mag change in (NUV–BP) color for solar-type stars, which is about 2–3 times larger than the change in the $v - \text{BP}$ color (Huang et al. 2023), about 5 times larger than the change in the $u - g$ color (Yuan et al. 2015b), and about 200 times larger than the change in the BP–G color (Xu et al. 2022a). This can be attributed to the prevalence of strong metal absorption lines in the NUV-band, leading to heightened sensitivity to metallicity, as expected. The fitting residuals, as a function of BP–RP, $[\text{Fe}/\text{H}]$, M_G , $E(B-V)$, and NUV are plotted in panels (c), (d), (e), (f), and (g), respectively. No trends are found. Panel (h) plots the histogram distribution of the fitting residuals. A Gaussian profile is fitted to the distribution, resulting in a narrow peak centered at 0.00 mag with a σ of 0.13 mag. The fitting results of the giant training sample are similar, and shown in Figure 6.

Based on the $[\text{Fe}/\text{H}]$ - and M_G -dependent stellar loci, we employ a minimum χ^2 technique to estimate the photometric metallicities from NUV–BP, BP–RP, and absolute magnitude M_G . The χ^2 is defined as:

$$\chi^2([\text{Fe}/\text{H}]) = \frac{[C_{\text{NUV-BP}}^{\text{int}} - C_{\text{NUV-BP}}^{\text{int}}(\text{BP-RP}, [\text{Fe}/\text{H}], M_G)]^2}{\sigma_{\text{NUV}}^2 + \sigma_{\text{BP}}^2}, (2)$$

where $C_{\text{NUV-BP}}^{\text{int}}$ is the intrinsic NUV–BP color, $C_{\text{NUV-BP}}^{\text{int}}(\text{BP-RP}, [\text{Fe}/\text{H}])$ represents the predicted intrinsic NUV–BP color based on the metallicity- and M_G -dependent stellar loci, and σ_{NUV}^2 and σ_{BP}^2 represent the magnitude uncertainties in NUV and BP, respectively. Indeed, σ_{BP}^2 could be safely ignored compared to σ_{NUV}^2 . We utilize a brute-force algorithm to determine the optimal $[\text{Fe}/\text{H}]$ value for each source. For a given dwarf, the $[\text{Fe}/\text{H}]$ value is varied from -4.0 to $+1.0$ with steps of 0.01 dex, resulting in 501 χ^2 values. For a given giant, the $[\text{Fe}/\text{H}]$ value is varied from -5.0 to $+1.0$ with steps of 0.01 dex. The minimum χ^2 among these values corresponds to the optimal $[\text{Fe}/\text{H}]$ value.

4. RESULTS AND DISCUSSION

We employed the above model and technique to determine the photometric-metallicity estimates, denoted as $[\text{Fe}/\text{H}]_{\text{GALEX}}$, based on the NUV–BP, BP–RP, and absolute magnitude M_G obtained from Gaia EDR3 and GALEX GR6+7 AIS datasets. In this section, we test and verify the accuracy and precision of our approach.

4.1. Results for the Training Sample

The photometric metallicities for the dwarf and giant training samples are presented in Figures 7 and 8, respectively. The residuals $\Delta[\text{Fe}/\text{H}]$, defined as

$\Delta[\text{Fe}/\text{H}] = [\text{Fe}/\text{H}]_{\text{GALEX}} - [\text{Fe}/\text{H}]_{\text{HR}}$, is used to assess the precision of our results here, where $[\text{Fe}/\text{H}]_{\text{HR}}$ is $[\text{Fe}/\text{H}]$ from high-resolution spectroscopy (PASTEL and SAGA). Panel (a) shows a histogram distribution of the $\Delta[\text{Fe}/\text{H}]$. The standard deviation of $\Delta[\text{Fe}/\text{H}]$ for the dwarf training sample is 0.16 dex, with a mean value of 0.01 dex. For the giant training sample, the standard deviation is 0.21 dex, with a mean value of 0.01 dex. Panel (b) shows the correlation between $[\text{Fe}/\text{H}]_{\text{GALEX}}$ and $[\text{Fe}/\text{H}]_{\text{HR}}$. Strong correlations are found for $[\text{Fe}/\text{H}]$ down to $[\text{Fe}/\text{H}] \sim -3.0$ for the dwarfs and to $[\text{Fe}/\text{H}] \sim -4.0$ for the giants. Panels (c), (d), (e), (f), (g) show the distributions of $\Delta[\text{Fe}/\text{H}]$ as a function of BP–RP color, $[\text{Fe}/\text{H}]_{\text{HR}}$, M_G , $E(B-V)$ and NUV, respectively. No discernible trends are found.

In panel (b) of Figure 7, at $[\text{Fe}/\text{H}] < -2.0$, the dispersion for dwarfs between $[\text{Fe}/\text{H}]_{\text{GALEX}}$ and $[\text{Fe}/\text{H}]_{\text{HR}}$ increases, corresponding to the sources in panel (h), whose color slightly deviates from $\Delta[\text{Fe}/\text{H}] = 0.0$. This is due to the fact that lower metallicity corresponds to a lower sensitivity of the stellar locus. Consequently, estimating precise photometric metallicities for very metal-poor (VMP; $[\text{Fe}/\text{H}] \leq -2.0$) and extremely metal-poor (EMP; $[\text{Fe}/\text{H}] \leq -3.0$) stars becomes challenging. This challenge is also evident for giants, though with slightly improved performance, as seen in panel (b) of Figure 8.

Panel (h) of Figure 7 and Figure 8 plots $\Delta[\text{Fe}/\text{H}]$ in the color-magnitude diagram. For dwarfs, most $\Delta[\text{Fe}/\text{H}]$ values are very close to zero. A small region with slight deviations from $\Delta[\text{Fe}/\text{H}] = 0$ is derived from the larger dispersion in the most metal-poor stars. Overall, $\Delta[\text{Fe}/\text{H}]$ has no significant structure associated with M_G , which is attributed to our consideration of M_G of our model. There is also no significant structure associated with M_G for giants. For some individual outliers, it is not meaningful to consider them due to the scarcity of these sources. We consider the outliers in our comparison with the test sample below.

4.2. External Tests with LAMOST DR8

In order to verify the accuracy of our model, some external checks are performed in this section by comparing with spectroscopic-metallicity measurements from LAMOST DR8. First, we cross-match the LAMOST DR8 data with GALEX GR6+7 AIS and Gaia EDR3. After application of the following cuts:

1. Signal-to-noise ratio for the g-band of the LAMOST spectra $\text{SNR}_g > 20$
2. Galactic latitude $|b| > 10^\circ$ and $E(B-V) \leq 0.5$

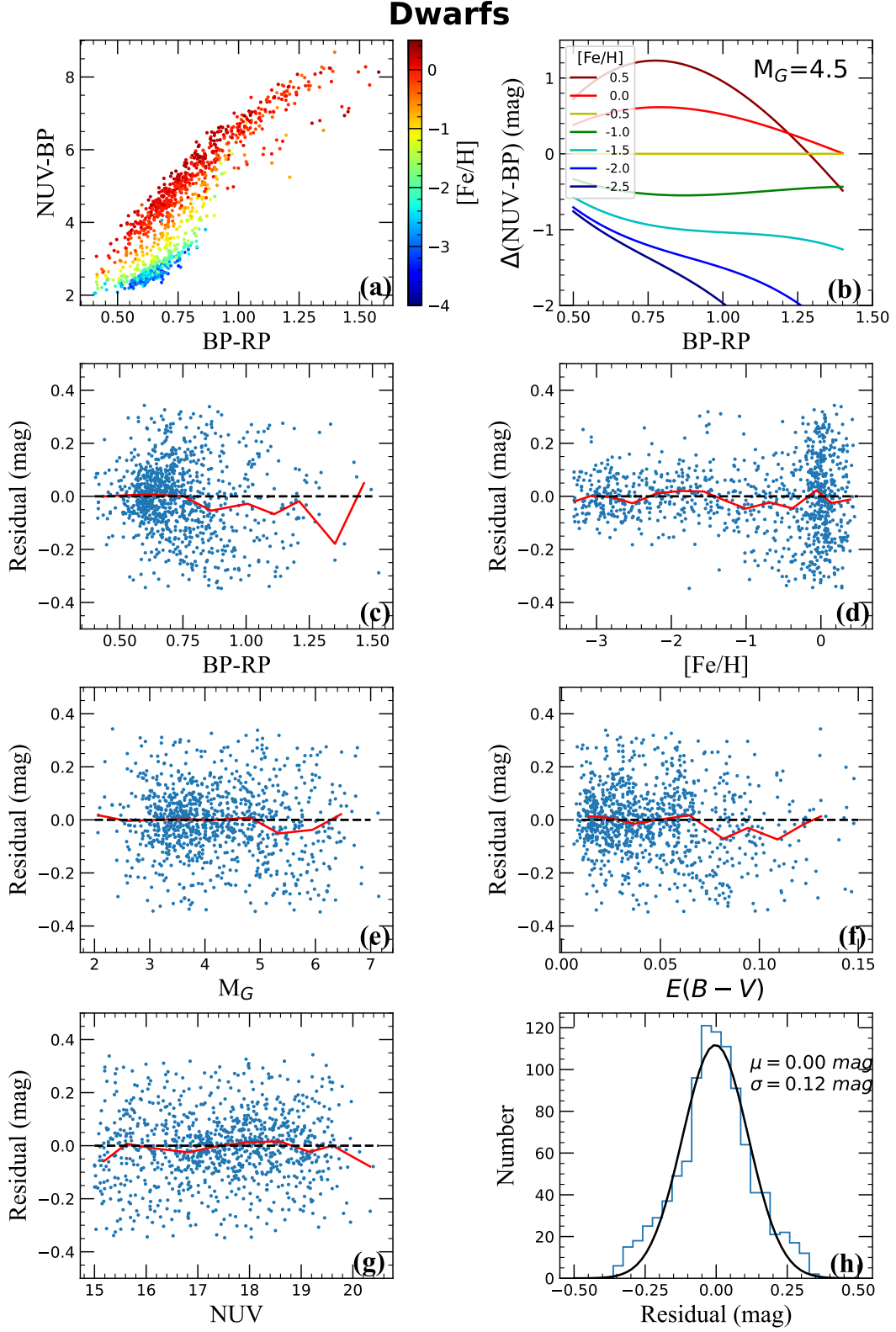


Figure 5. Panel (a): Distributions of the dwarf training sample in the NUV–BP vs. BP–RP plane (stellar loci), color-coded by $[\text{Fe}/\text{H}]$ as shown in the right color bar. Panel (b): When $M_G = 4.5$, the variations of stellar loci for different metallicities (as shown in the label) relative to the one at $[\text{Fe}/\text{H}] = -0.5$. Panels (c–g): Fitting residuals as a function of BP–RP color, $[\text{Fe}/\text{H}]$, M_G , $E(B-V)$, and NUV, respectively. Panel (h): Histogram distribution of the fitting residuals, with the Gaussian fitting profile over-plotted in black.

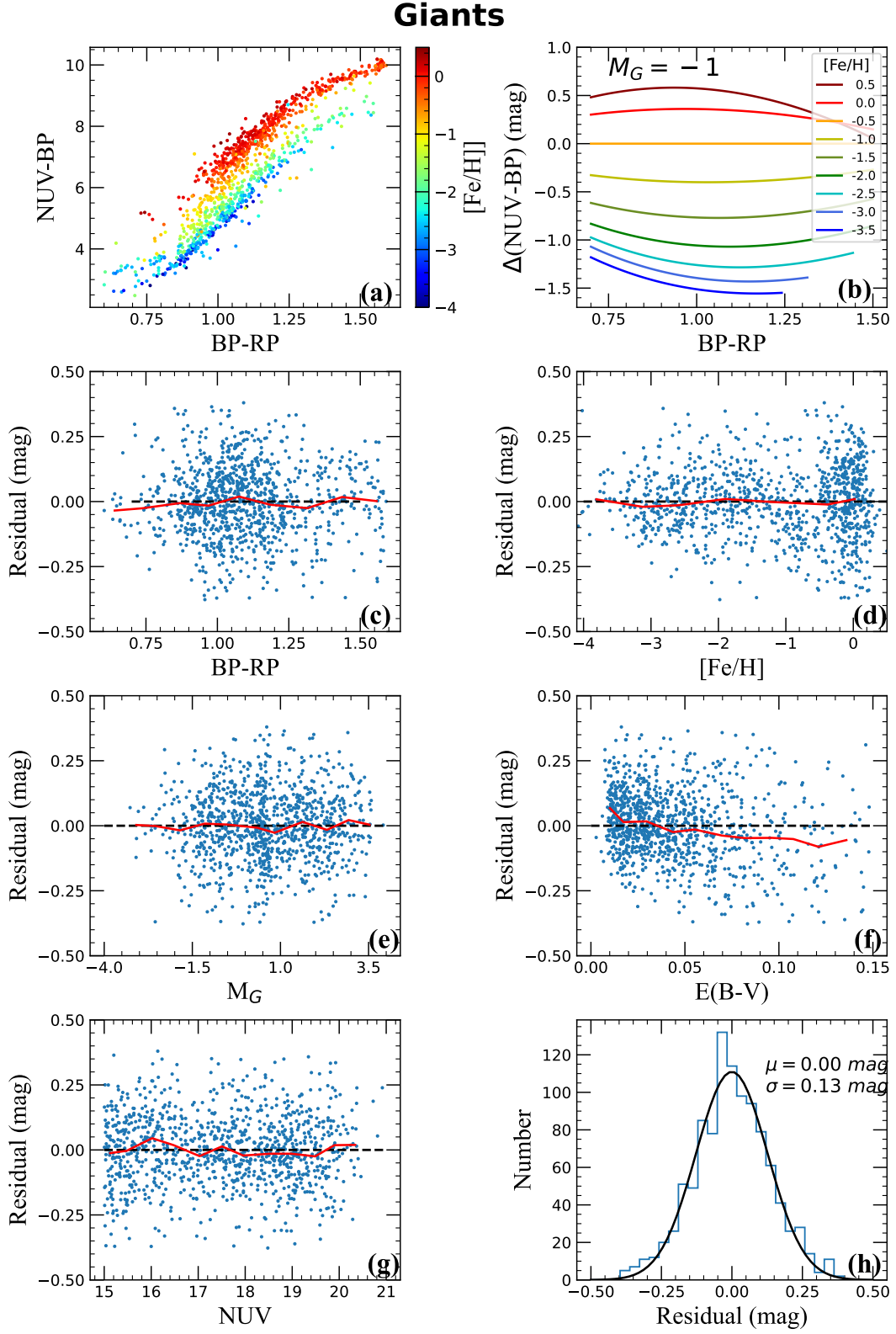


Figure 6. Same as Figure 5, but for the giant training sample.

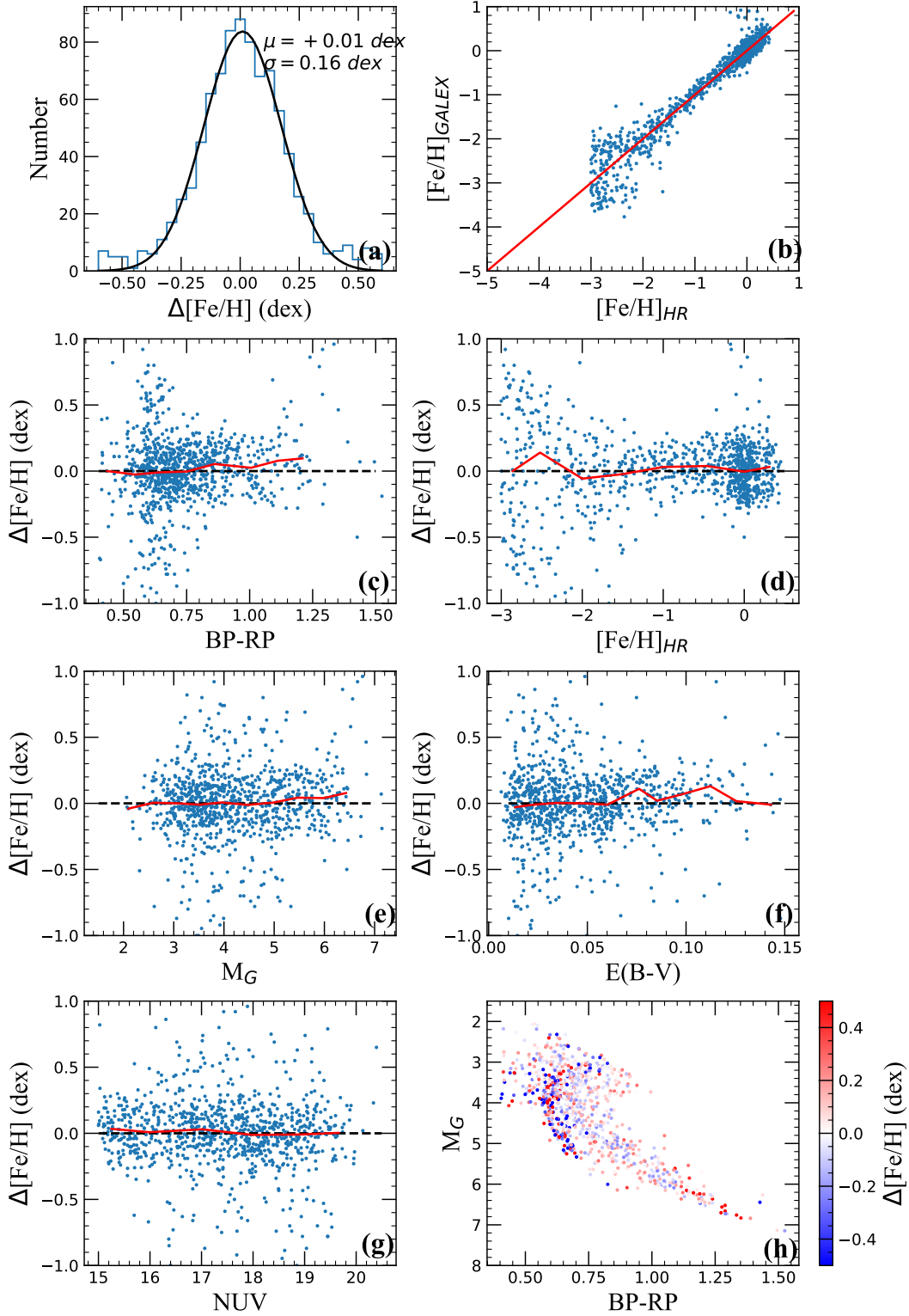
Dwarfs

Figure 7. Photometric metallicities for the dwarf training sample. Panel (a): Histogram distribution of the residuals $\Delta[\text{Fe}/\text{H}]$, with the Gaussian fitting profile over-plotted in black. Panel (b): Comparison of photometric-metallicity estimates from GALEX and Gaia data with high-resolution spectroscopic metallicities from SAGA or PASTEL. Panels (c)–(g): $\Delta[\text{Fe}/\text{H}]$ as a function of BP–RP color, $[\text{Fe}/\text{H}]_{\text{HR}}$, M_G , $E(B-V)$, and NUV, respectively. Panel (h): The color-magnitude diagram, color-coded by $\Delta[\text{Fe}/\text{H}]$.

Giants

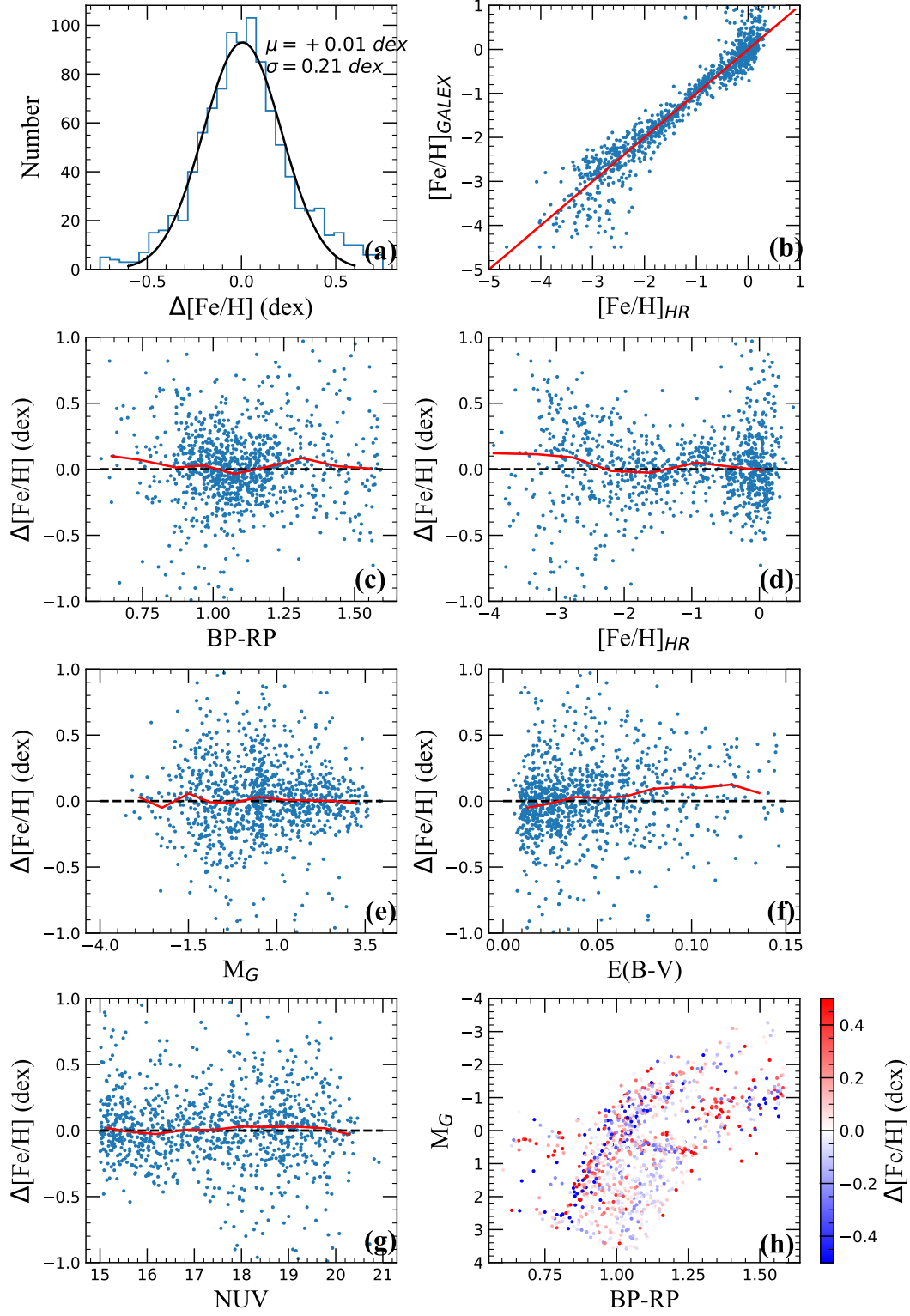


Figure 8. Same as Figure 7, but for the giant training sample.

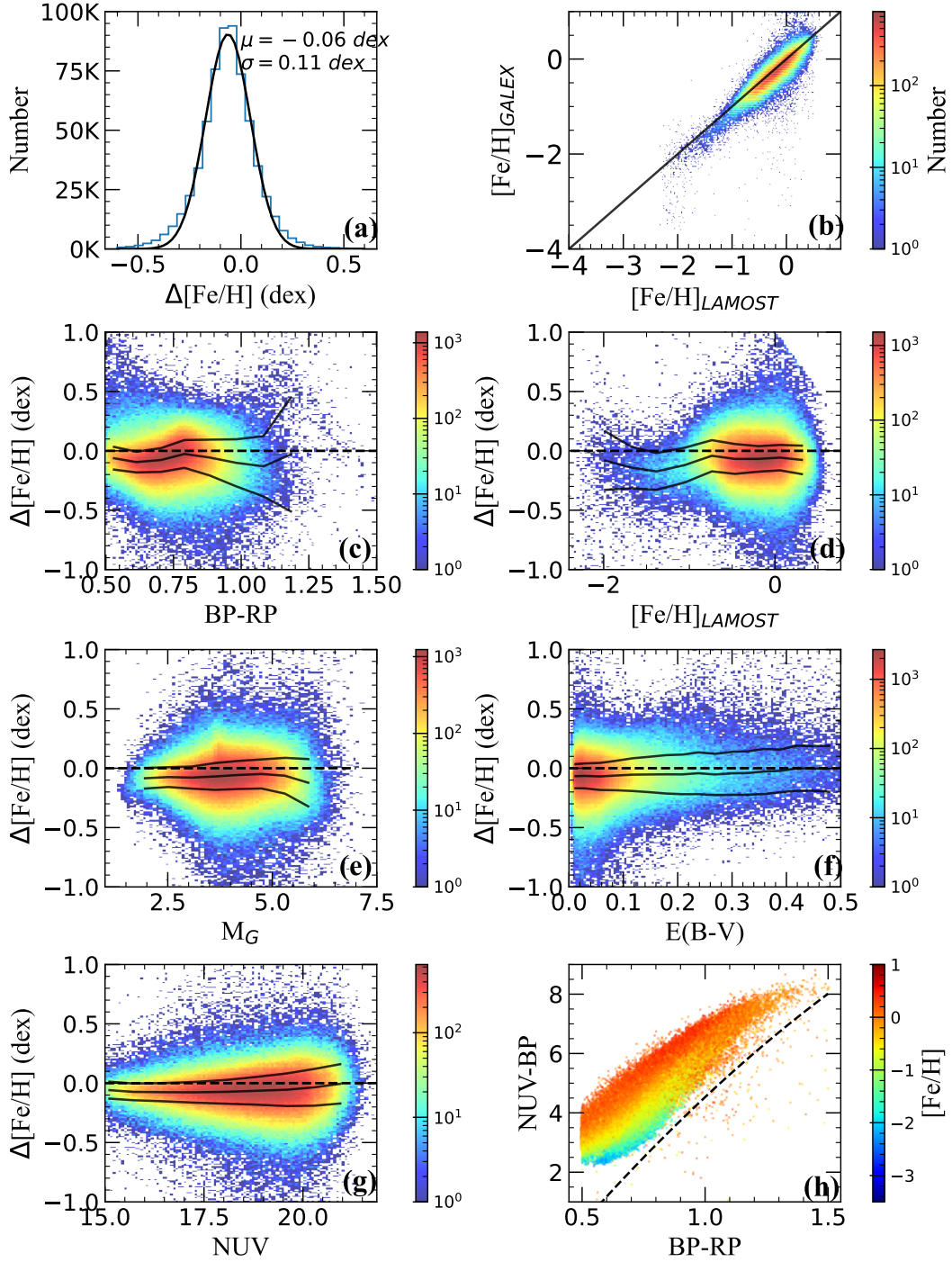
Dwarfs

Figure 9. Test results for 633,807 dwarfs. Panel (a): Histogram distribution of the residuals $\Delta[\text{Fe}/\text{H}]$, with the mean and standard deviation values labeled. Panel (b): $[\text{Fe}/\text{H}]_{\text{GALEX}}$ as a function of $[\text{Fe}/\text{H}]_{\text{LAMOST}}$, color-coded by number density. Panel (c), (d), (e), (f), (g): $\Delta[\text{Fe}/\text{H}]$ as a function of BP-RP color, $[\text{Fe}/\text{H}]_{\text{LAMOST}}$, M_G , $E(B-V)$, and NUV, respectively. The black-solid lines indicate the median values and standard deviations. The black-dashed line indicates the zero level. Panel (h): Distributions of the dwarfs in the $(\text{NUV} - \text{BP})$ vs. $(\text{BP} - \text{RP})$ plane, color-coded by $[\text{Fe}/\text{H}]$ values from LAMOST, as indicated by the right color bar. The expression for the black-dashed line is: $(\text{NUV} - \text{BP}) < -1.56 \times (\text{BP} - \text{RP})^2 + 10.87 \times (\text{BP} - \text{RP}) - 4.78$ for dwarfs.

Giants

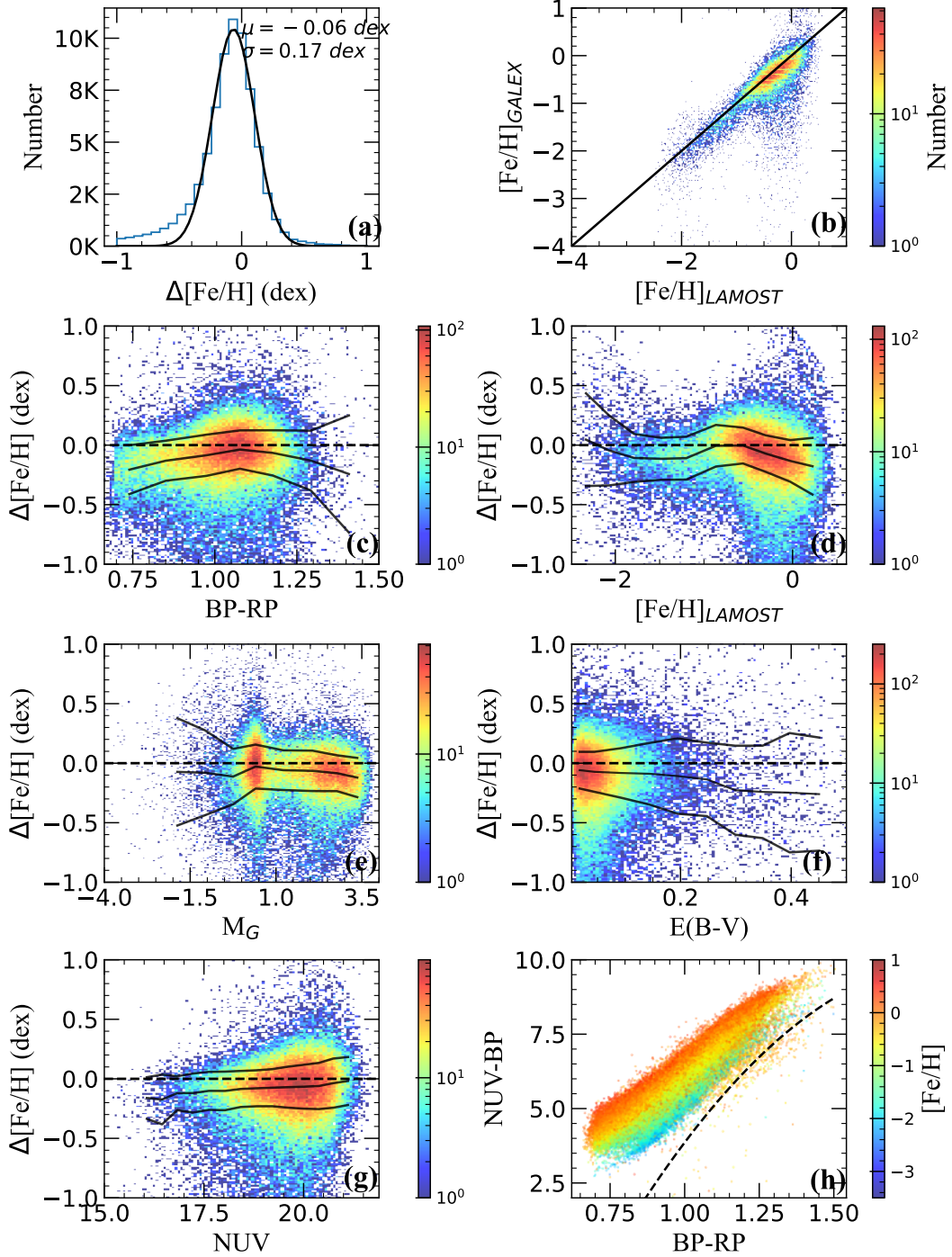


Figure 10. Same as Figure 9, but for 72,911 giants. The expression for the black-dashed line is: $(\text{NUV} - \text{BP}) < -7.20 \times (\text{BP} - \text{RP})^2 + 27.69 \times (\text{BP} - \text{RP}) - 16.63$.

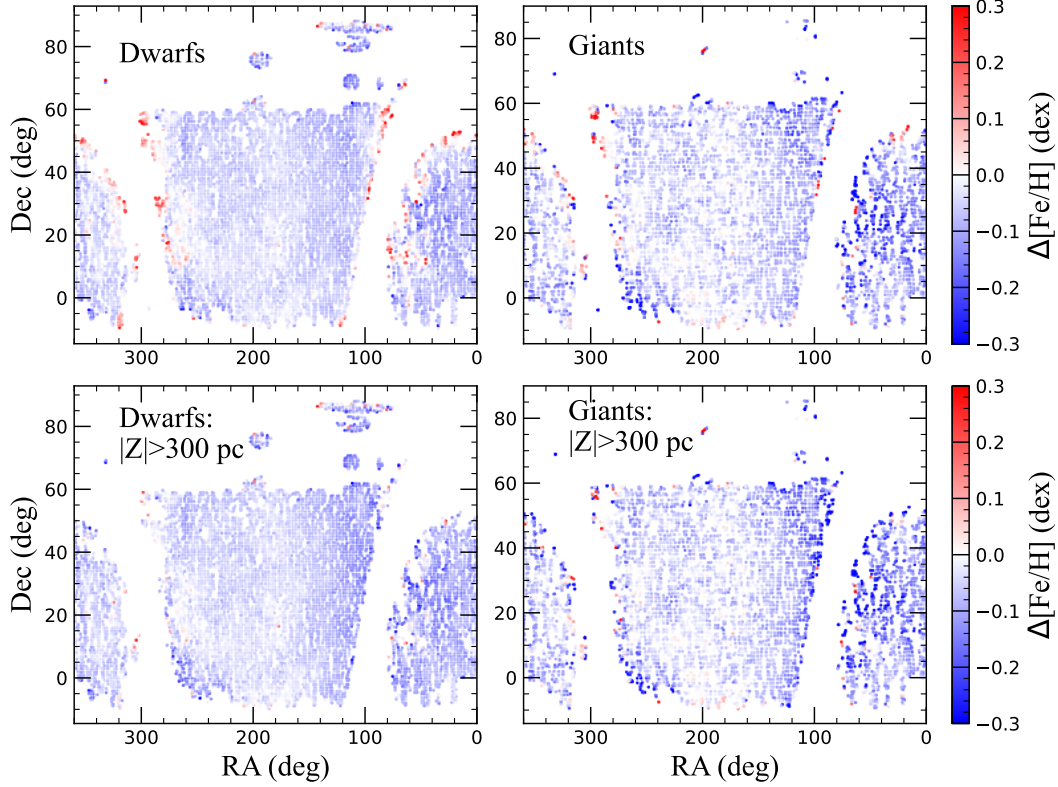


Figure 11. The spatial distribution (RA and Dec) of the residuals $\Delta[\text{Fe}/\text{H}]$. The top row of panels are for the test-with-LAMOST sample of 633,807 dwarfs and 72,911 giants, respectively. The bottom row of panels are the sub-sample of these stars with $|Z| > 300$ pc (441,141 dwarfs and 64,696 giants, respectively.)

3. Sources with $10 < G \leq 16$ and within the limits of BP–RP color and phot_bp_rp_excess_factor (the same as Xu et al. 2022a),

we retain a sample with 633,807 dwarfs and 72,911 giants. The comparison results are displayed in Figures 9, 10, and 11. Note that there are small metallicity offsets between the LAMOST and training sample: -0.07 dex for dwarfs, and -0.06 dex for giants. The residual $\Delta[\text{Fe}/\text{H}]$ is defined as: $\Delta[\text{Fe}/\text{H}] = [\text{Fe}/\text{H}]_{\text{GALEX}} - [\text{Fe}/\text{H}]_{\text{LAMOST}}$.

For the dwarfs in Figure 9, we fit the histogram distribution of the residuals $\Delta[\text{Fe}/\text{H}]$ with a Gaussian profile, and obtain a small standard deviation of only 0.11 dex, centered at -0.06 dex, as shown in panel (a). Panel (b) shows the relationship between $[\text{Fe}/\text{H}]_{\text{GALEX}}$ and $[\text{Fe}/\text{H}]_{\text{LAMOST}}$. Most sources exhibit good agreement between $[\text{Fe}/\text{H}]_{\text{GALEX}}$ and $[\text{Fe}/\text{H}]_{\text{LAMOST}}$, except for a tiny fraction of sources located at the bottom right, which could be due to stellar activity in the NUV-band. From inspection of panels (c–g), we conclude that the $\Delta[\text{Fe}/\text{H}]$ values exhibit no discernible trends with BP–RP color, $[\text{Fe}/\text{H}]_{\text{LAMOST}}$, M_G , $E(B-V)$, and NUV. Panel (h) shows the distributions of the 633,807 dwarfs in the NUV–BP vs. BP–RP plane, color-coded by

$[\text{Fe}/\text{H}]_{\text{LAMOST}}$. The black-dashed line is used to separate the outliers. From inspection, there are some cooler metal-rich stars located below the black-dashed line, we assume due to stellar activity. These sources would be miss-classified as metal-poor stars in our model.

For the giants in Figure 10, the dispersion of the residuals $\Delta[\text{Fe}/\text{H}]$ is 0.17 dex, with a mean value of -0.06 dex, as shown in panel (a). As indicated by the relationship between $[\text{Fe}/\text{H}]_{\text{GALEX}}$ and $[\text{Fe}/\text{H}]_{\text{LAMOST}}$ in panel (b), the majority of sources also exhibit good agreement between $[\text{Fe}/\text{H}]_{\text{GALEX}}$ and $[\text{Fe}/\text{H}]_{\text{LAMOST}}$. However, there are more outliers located at the bottom right compared to the dwarfs. This could be due to more stellar activity in cool giants, leading to a decrease in the NUV magnitude and lower $[\text{Fe}/\text{H}]_{\text{GALEX}}$ values. In panels (c–g), there are some subtle trends in the residuals worth discussing. In panel (c), the median value of $\Delta[\text{Fe}/\text{H}]$ is slightly smaller at bluer and redder BP–RP colors, which is mainly attributed to the scarcity of bluer and redder BP–RP sources in our training sample. The result of panel (d) is similar to that shown in panel (b). Panel (e) shows that the errors are larger for intrinsically brighter stars. Panel (f) shows that both the median differences and errors increase as $E(B-V)$ increases. While the errors display very weak dependence

on NUV magnitude, as shown in panel (g), and also seen in the dwarfs. Panel (h) shows the distributions of the 72,911 giants in the NUV–BP vs. BP–RP plane, color-coded by $[\text{Fe}/\text{H}]_{\text{LAMOST}}$. The black-dashed line is used to separate the outliers.

Figure 11 shows the spatial distribution of the residuals $\Delta[\text{Fe}/\text{H}]$. Due to the over-estimation of extinction values in the SFD98 reddening map close to the Galactic plane, there is an over-estimation of $[\text{Fe}/\text{H}]$ in our model for the stars in this region, as shown in the top row of panels (especially in dwarfs). We can eliminate this over-estimation from SFD98 by applying a $|Z| > 300$ pc cut, as shown in the bottom row of panels.

4.3. Additional Tests

Comparisons with other independent stellar-metallicity measurements (spanning a wide range of $[\text{Fe}/\text{H}]$ values) are presented in this section. Four catalogs are used here: the value-added catalog of LAMOST DR8 (Wang et al. 2022), the SEGUE DR12 (Alam et al. 2015) catalog, the catalog of 10,000 VMP stars from LAMOST DR3 (Li et al. 2018), and the 400 VMP metal-poor stars studied with LAMOST and Subaru (Li et al. 2022). To perform the comparisons, we cross-match these catalogs with the Gaia EDR3 and GALEX GR6+7 AIS catalogs, respectively. We retain the sources after applying the criteria similar to those used for the LAMOST DR8 test sample. The results are presented in Figure 12, with the top panels for dwarfs and the bottom panels for giants.

In the left column of panels, we show the comparison with the LAMOST DR8 value-added catalog. $[\text{Fe}/\text{H}]_{\text{PASTEL\&VMP}}$ represents $[\text{Fe}/\text{H}]_{\text{PASTEL}}$ (for $[\text{Fe}/\text{H}] > -1.5$) and $[\text{Fe}/\text{H}]_{\text{VMP}}$ (for $[\text{Fe}/\text{H}] < -1.5$) from Wang et al. (2022). The residuals between the $[\text{Fe}/\text{H}]_{\text{GALEX}}$ and $[\text{Fe}/\text{H}]_{\text{PASTEL\&VMP}}$ were fitted with a Gaussian profile. For dwarfs, we obtain a dispersion of 0.15 dex centered at -0.08 dex. For giants, a dispersion of 0.21 dex centered at -0.06 dex is obtained. The middle column of panels displays the comparison with SEGUE DR12. For dwarfs, we obtain a dispersion of 0.16 dex centered at -0.11 dex. For giants, a dispersion of 0.25 dex centered at -0.07 dex is obtained. The right column of panels displays the comparison with the catalogs of Li et al. (2018, 2022). For dwarfs, we obtain a dispersion of 0.25 dex centered at $+0.29$ dex. For giants, the dispersion is 0.26 dex centered at $+0.19$ dex. From inspection, our $[\text{Fe}/\text{H}]$ measurements exhibit good consistency with other catalogs for most sources, both for metal-rich stars and VMP stars.

There are a few sources with $[\text{Fe}/\text{H}]_{\text{GALEX}}$ values larger than $[\text{Fe}/\text{H}]_{\text{obs}}$ located in the upper part of the

right panels of Figure 12. Their locations in the color-color diagram are close to the metal-rich stellar loci, probably due to their large photometric errors. In addition, there is an under-estimation of $[\text{Fe}/\text{H}]$ in our model for a portion of sources with $[\text{Fe}/\text{H}]_{\text{GALEX}}$ values lower than -3.0 , as can be mainly seen in the bottom middle panel of Figure 12. This is because the metallicity dependence decreases monotonically as NUV–BP color decreases at the same BP–RP color. Thus, between the over-estimates or under-estimates of NUV–BP colors caused by photometric errors, the under-estimates lead to a larger under-estimation in the calculation of photometric metallicities. Overall, from these tests, $[\text{Fe}/\text{H}]$ estimates from our model are reliable even for metallicity down to $[\text{Fe}/\text{H}] \sim -3.5$.

4.4. The Influence of Carbon Enhancement

Photometric-metallicity measurements are often over-estimated for VMP/EMP stars due to contamination of the blue narrow/medium-band filters by molecular carbon bands such as CN (e.g., Hong et al. 2023, Huang et al. 2023). In this subsection, we check whether the strong molecular carbon bands strongly influence the photometric-metallicity estimates found by use of the NUV-band. We cross-match the medium- and high-resolution spectroscopic catalog of VMP/EMP stars with available $[\text{Fe}/\text{H}]$ and $[\text{C}/\text{Fe}]$ measurements compiled by Hong et al. (2023) with our Gaia EDR3 and GALEX GR6+7 AIS catalog. After applying metallicity cuts of $-4 < [\text{Fe}/\text{H}]_{\text{spec}} \leq -2$, $[\text{Fe}/\text{H}]_{\text{GALEX}} > -4$, and $\text{flag} = 0$, we obtain a sample of 231 stars in common.

Figure 13 shows comparisons of the photometric-metallicity estimates we obtain with the spectroscopic determinations, color-coded by $[\text{C}/\text{Fe}]$. The $[\text{Fe}/\text{H}]_{\text{spec}}$ and $[\text{C}/\text{Fe}]$ values are originally from Yoon et al. (2016), Li et al. (2022), Placco et al. (2022), and Zepeda et al. (2023). Figure 14 is a color-magnitude diagram for the VMP/EMP samples of stars with $[\text{C}/\text{Fe}] \leq +0.7$ and $[\text{C}/\text{Fe}] > +0.7$, indicated by red and blue symbols, respectively.

From inspection of Figure 13, all three samples exhibit a good correlation between $[\text{Fe}/\text{H}]_{\text{GALEX}}$ and $[\text{Fe}/\text{H}]_{\text{spec}}$, with small offsets. Note that the dispersion value is larger for the sub-sample of stars with $[\text{C}/\text{Fe}] > +0.7$ than for the sub-sample with $[\text{C}/\text{Fe}] < +0.7$. This is likely due to 1) the fact that the sub-sample of stars with $[\text{C}/\text{Fe}] > +0.7$ are bluer (and less sensitive to $[\text{Fe}/\text{H}]$) and fainter (larger photometric errors), and thus have larger uncertainties in the $[\text{Fe}/\text{H}]_{\text{GALEX}}$ estimates and, 2) the effects of carbon enhancement on our estimates, primarily for the cooler giants in our sample. However, we point out that, for all three samples, there are stars

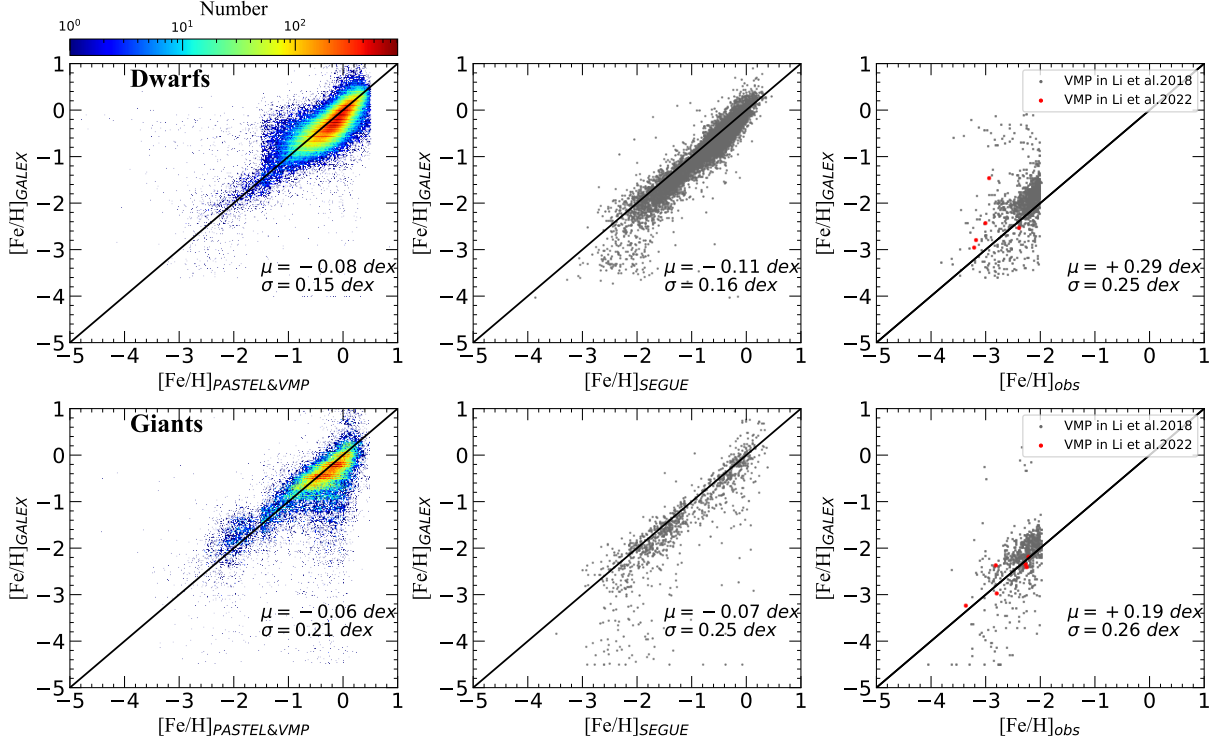


Figure 12. From left to right, the columns of panels represent comparisons with the LAMOST DR8 value-added catalog of Wang et al. (2022), the SEGUE DR12 (Alam et al. 2015) catalog, and the VMP catalog of Li et al. (2018) & Li et al. (2022), respectively. The left column of panels is color-coded by the source number density. In the right column of panels, the red and gray dots are from Li et al. (2022) and Li et al. (2018), respectively. The dwarfs are plotted in the top row of panels and the giants in the bottom row of panels. The mean and standard deviation values of the residuals $\Delta[\text{Fe}/\text{H}]$ are labeled in the lower-right of each panel.

with photometric-metallicity estimates that straddle the one-to-one line, which is superior to the behavior seen by Hong et al. (2023) when comparing to photometric-metallicity estimates obtained using the u- and v-band filters from the SAGES and SMSS samples (see their Figure A1, where the carbon-enhanced stars often result in higher-metallicity estimates than their spectroscopic values). A similar problem is encountered in the analysis of Martin et al. (2023), which used the Gaia XP spectra in combination with synthetic photometry of the Pristine survey CaHK magnitudes (see Martin et al. 2023).

Thus, we conclude that the addition of the NUV-band can provide for improved estimates of photometric metallicity for stars with strong carbon enhancements. Clearly, having an independent estimate of $[\text{C}/\text{Fe}]$, as is possible with the filter sets used by J-PLUS and S-PLUS, would provide an even better alternative.

5. THE FINAL SAMPLE

In this section, we cross-match the entire Gaia EDR3 data and GALEX GR6+7 AIS data to create our (nearly) all-sky sample. After imposing the following selection criteria:

1. GALEX: $\text{error}_{\text{NUV}} < 0.15$ and $\text{NUV} > 15$ to avoid saturation
2. Gaia (same as Xu et al. 2022a except that we extend the bright G magnitude limit to 6): sources of $|b| > 10^\circ$, $E(B-V) \leq 0.5$, $6 < G < 16$, and limit on $\text{phot_bp_rp_excess_factor}$ and BP-RP color,

4,468,105 dwarfs and 503,700 giants remain in our final sample (4,971,805 stars in all). The color-magnitude diagram for this sample is shown in Figure 15. The G-magnitude distributions of the final sample (with $\text{flag}=0$) are shown in Figure 16.

We apply our model to this final sample. The $[\text{Fe}/\text{H}]$ (with $\text{flag}=0$) distributions are shown in Figure 17. The increase in the numbers of stars at the minimum $[\text{Fe}/\text{H}]$ values is due to 1) the metallicities in our model can only be reliably determined in a range of $-4.0 < [\text{Fe}/\text{H}] \leq +1.0$ for dwarfs and $-4.5 < [\text{Fe}/\text{H}] \leq +1.0$ for giants, respectively, which resulting in an accumulation at the boundary of the range and, 2) there still remain stars with stellar activity, although we have applied a flag in an attempt to filter them out. For dwarfs, there are 14,528 VMP and 2,972 EMP and stars, respectively.

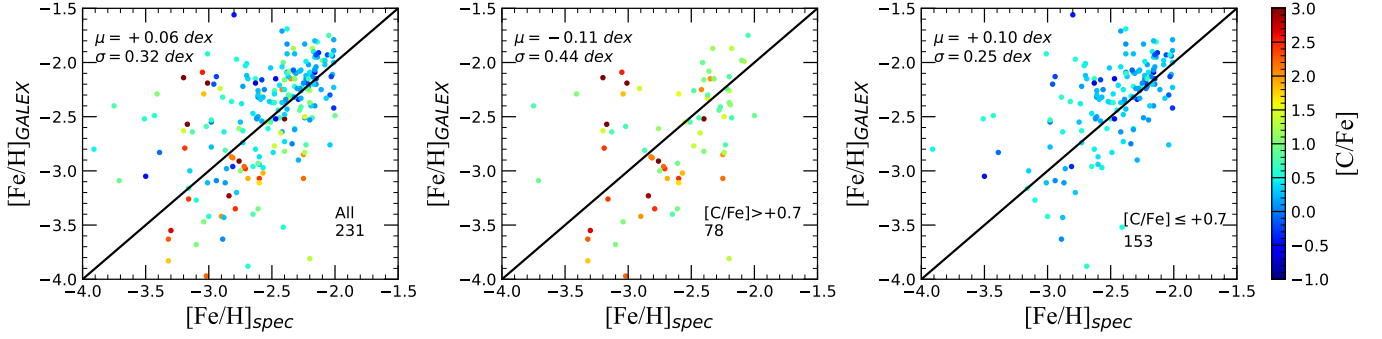


Figure 13. Comparisons of $[\text{Fe}/\text{H}]_{\text{GALEX}}$ with spectroscopic measurements for VMP/EMP stars (taken from the compilation of Hong et al. 2023), color-coded by $[\text{C}/\text{Fe}]$. From left to right the panels show the full sample, the sub-sample of stars with $[\text{C}/\text{Fe}] > +0.7$, and the sub-sample of stars with $[\text{C}/\text{Fe}] \leq +0.7$, respectively. The mean and standard deviation values of residuals $\Delta[\text{Fe}/\text{H}]$ are labeled in the upper-left of each panel. Note that, in all three panels, there are stars with $[\text{Fe}/\text{H}]_{\text{GALEX}}$ that straddle the black-solid one-to-one lines; they are *not* uniformly biased high due to the effect of carbon, as has been seen to occur for several previous photometric-metallicity techniques (see text).

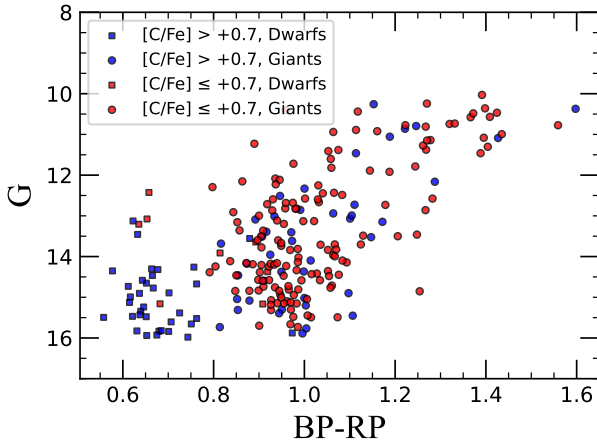


Figure 14. Color-magnitude (observed color and apparent magnitude) diagram for sub-samples of the VMP/EMP stars shown in Figure 13, represented by the red ($[\text{C}/\text{Fe}] \leq +0.7$) and blue ($[\text{C}/\text{Fe}] > +0.7$) symbols, respectively. The squares and circles represent dwarfs and giants, respectively.

For giants, there are 18,747 VMP and 3,656 EMP stars, respectively.

The spatial distributions in the Z-R plane are shown in Figure 18, where Z is the distance to the Galactic plane, and R is the Galactocentric distance. The spatial distributions, color-coded by $[\text{Fe}/\text{H}]$, are shown in Figure 19. The evident vertical gradients in metallicity within the disk-system stars are observable in both panels.

The columns contained in the final sample catalog are listed in Table 2. Similar to Huang et al. (2023), the radial-velocity values in the catalog are collected from five spectroscopic surveys: GALAH DR3+ (Buder et al. 2021), SDSS/ APOGEE DR17 (Abdurro’uf et al.

2022), Gaia DR3 (Katz et al. 2023), LAMOST DR9² and SDSS/SEGUE DR16 (Ahumada et al. 2020). In total, over 4,702,675 stars in our final sample have radial-velocity measurements. When a star has two more radial-velocity measurements, we adopt the results from the highest spectral resolution survey. Note that we calibrated all of the radial-velocity offsets based on the APOGEE radial-velocity values. The catalog is publicly available at xxxx.

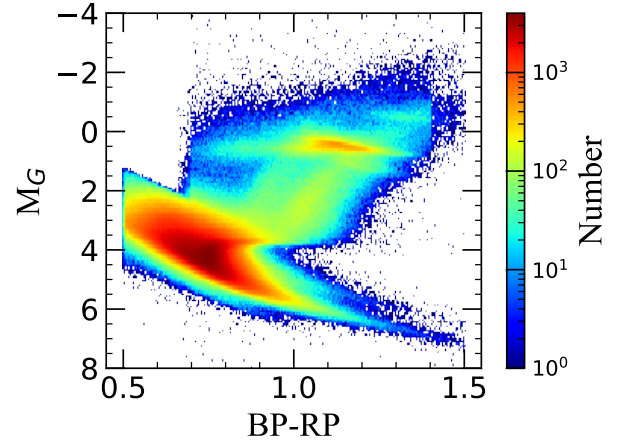


Figure 15. Color-magnitude diagram of the final sample, color-coded by source number density.

6. SUMMARY

In this work, we combine the SAGA and PASTEL catalogs with Gaia EDR3 and GALEX GR6+7 AIS data as our training sample to construct a relational model

² <http://www.lamost.org/dr9/v1.0/> (medium resolution catalog and low resolution catalog)

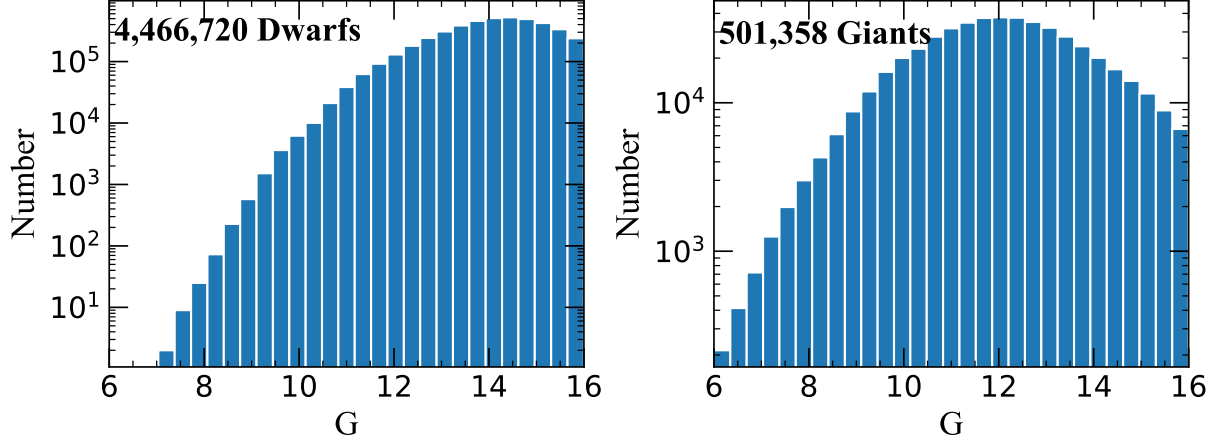


Figure 16. The G-magnitude distribution of the final sample (with flag=0). The left and right panels are for the dwarfs and giants, respectively.

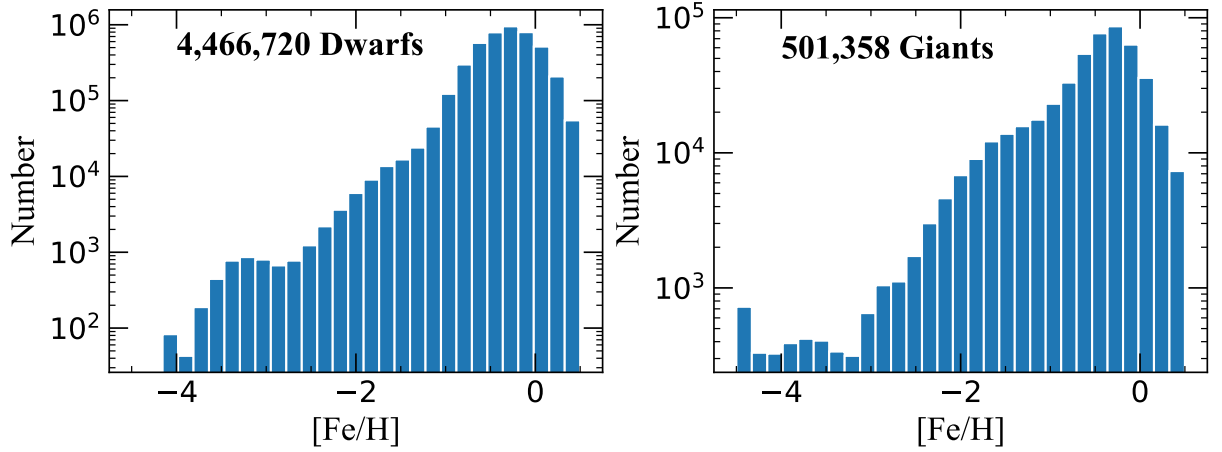


Figure 17. The $[\text{Fe}/\text{H}]$ distribution of the final sample (with flag=0). The left and right panels are for the dwarfs and giants, respectively. For dwarfs, there are 14,522 VMP and 2,962 EMP stars, respectively. For giants, there are 18,245 VMP and 3,582 EMP stars, respectively. Note that the increase in the numbers of stars at the lowest metallicities are due to limitations of our model and the likely presence of stellar activity (see text).

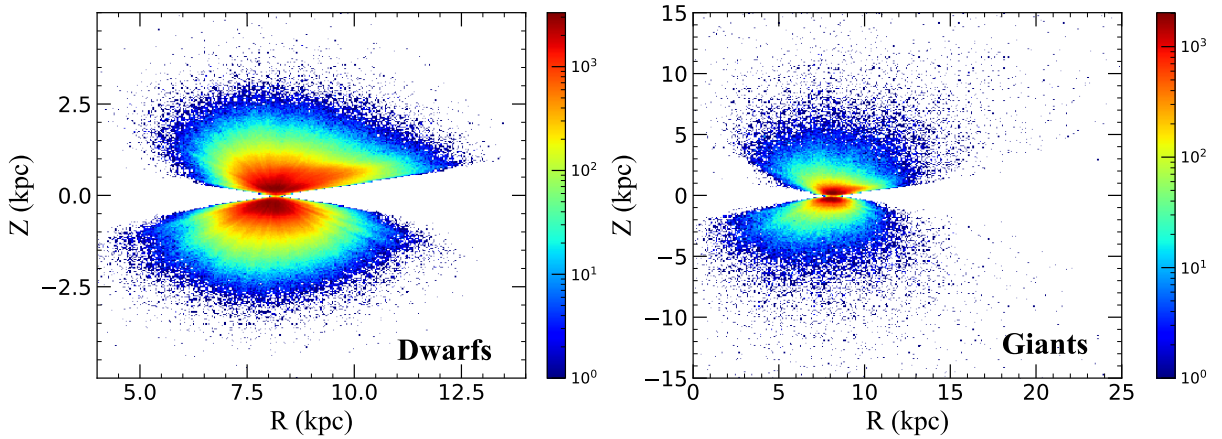


Figure 18. The spatial distributions in the Z-R plane of the final sample, color-coded by number densities. The left and right panels are for the dwarfs and giants, respectively. The Sun is located at $(R, Z) = (8.178, 0.0)$ kpc.

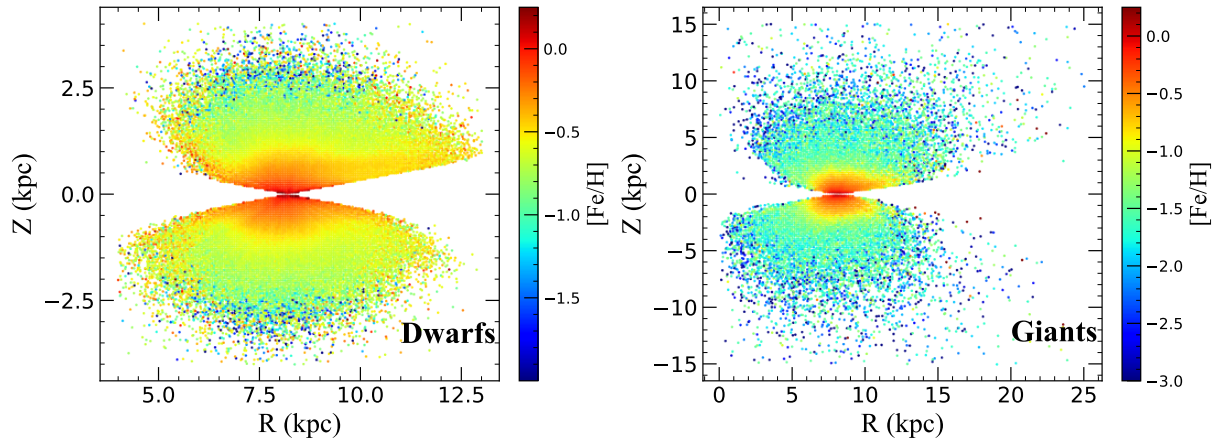


Figure 19. The spatial distributions in the Z–R plane of the final sample, color-coded by $[Fe/H]_{\text{GALEX}}$. The left and right panels are for the dwarfs and giants, respectively. The Sun is located at $(R, Z) = (8.178, 0.0)$ kpc.

Table 2. Description of the Final Sample

Field	Description	Unit
source_id	Unique source identifier for Gaia EDR3 (unique with a particular Data Release)	–
ra	Right ascension from Gaia	deg
dec	Declination from Gaia	deg
parallax	Parallax	mas
parallax_error	Standard error of parallax	mas
parallax_corrected	Parallax corrected by Lindegren et al. (2021)	mas
pmra	Proper motion in right ascension direction	mas/year
pmra_error	Standard error of proper motion in right ascension direction	mas/year
pmdec	Proper motion in declination direction	mas/year
pmdec_error	Standard error of proper motion in declination direction	mas/year
ruwe	Renormalised unit weight error	–
phot_bp_rp_excess_factor	BP/RP excess factor	–
phot_bp_mean_mag	Integrated BP-band mean magnitude	–
phot_rp_mean_mag	Integrated RP-band mean magnitude	–
phot_g_mean_mag	G-band mean magnitude	–
l	Galactic longitude	deg
b	Galactic latitude	deg
feh_gaia	Photometric metallicity from Xu et al. (2022a)	–
feh_Gaia_error	Formal error of feh_gaia from Xu et al. (2022a)	dex
ebv	Value of $E(B - V)_{\text{SFD}}$	–
type	Flag to classify stars (Xu et al. 2022a); 0 for dwarfs and 1 for giants	–
NUVmag	NUV calibrated magnitude	–
e_NUVmag	NUV calibrated magnitude error	mag
BP_RP0	Intrinsic BP–RP color after color correction	–
NUV_BP0	Intrinsic NUV–BP color after color correction	–
feh_GALEX_old	Photometric metallicity derived from previous model without consideration of M_G	–
feh_GALEX	Photometric metallicity derived from New Model with consideration of M_G	–
M_G	Absolute Magnitude of G-band, calculated by: $M_G = G - 10 - 5 \times \log_{10} \frac{1}{\text{parallax_corrected}} - R_G \times E(B - V)$	–
flag ¹	The quality flag	–
rpgeo	Median of the photogeometric distance posterior ($r_{\text{med_photgeo}}$) from Bailer-Jones et al. (2021)	pc
b_rpgeo	16th percentile of the photogeometric distance posterior ($r_{\text{lo_photgeo}}$) from Bailer-Jones et al. (2021)	pc
B_rpgeo	84th percentile of the photogeometric distance posterior ($r_{\text{lo_photgeo}}$) from Bailer-Jones et al. (2021)	pc
rv	Radial velocity	km/s
e_rv	Error of radial velocity	km/s
flag_rv	Flag to indicate the source of radial velocity, which takes the values “GALAH,” “APOGEE,” “Gaia,” “LAMOST_MRS,” “LAMOST_LRS,” “SEGUE”	–

NOTE— The flag takes the values of 0 or 1. ‘flag=1’ means the stars outside the limits where we consider the feh_GALEX values to be reliable. ‘flag=0’ means the stars are within the limits, and considered reliable.

from stellar loci that incorporate M_G to estimate photometric metallicities for dwarfs and giants. We construct an all-sky sample from Gaia EDR3 and GALEX GR6+7 AIS data as our final sample (4,468,105 dwarfs and 503,700 giants), employing a precise reddening correction using empirical temperature- and extinction-dependent extinction coefficients.

We first obtain the [Fe/H]- and M_G -dependent stellar loci for the NUV–BP and BP–RP colors. For a given BP – RP color, a 1 dex change in [Fe/H] causes an approximate 1 mag change in NUV – BP color for solar-type stars. The [Fe/H]- and M_G -dependent stellar

loci are then used to estimate stellar photometric metallicities from NUV – BP, BP–RP, and M_G . As a result of the very strong metallicity dependence in the NUV-band and the precise reddening corrections, we have obtained a typical precision of 0.11 dex for dwarfs and 0.17 dex for giants, with an effective metallicity range from $-3.0 < [\text{Fe}/\text{H}] \leq +0.5$ for dwarfs and $-4.0 < [\text{Fe}/\text{H}] \leq +0.5$ for giants. We also demonstrate that the NUV-band based photometric-metallicity estimate is not as strongly affected by carbon enhancement as previous photometric techniques. Moreover, our tests confirm that incorporating absolute magnitude (M_G) in

the stellar loci serves to further improve the accuracy of the photometric-metallicity estimates.

Our work demonstrates the feasibility and great potential of photometric-metallicity estimates using the NUV-band photometry, due to its very strong sensitivity to $[\text{Fe}/\text{H}]$. A number of lessons have been learned in this exploration, including:

1. The NUV-band photometry also exhibits a strong dependence on surface gravity, therefore, the absolute magnitude (M_G in this work) has to be taken into account in the modeling
2. The reddening correction in the NUV-band is essential and challenging. In addition to the effect of surface gravity, even the effect of metallicity on the extinction coefficient needs to be considered
3. Stellar activity in cool dwarf and giant stars could cause a significant under-estimation of metallicity, thus should be considered when hunting for VMP/EMP stars
4. Future improvement in the calibration precision of the NUV-band photometry is very important
5. With future improvement in the calibration precision in the NUV-band photometry, it may be possible to identify likely carbon-enhanced VMP/EMP stars by a comparison of photometric-metallicity estimates based on the NUV-band with other bands, such as the u- and v-bands.

Our final sample, encompassing a wide range of $[\text{Fe}/\text{H}]$ values, is expected to be valuable for numerous research studies. For instance, it can provide candidate metal-poor candidate stars for subsequent high-resolution spectroscopic follow-up, and also for chemodynamical studies of MW stellar populations. This work lays the foundation for using NUV-band data from space telescopes such as the upcoming Chinese Space Station Telescope (CSST; Zhan 2011).

This work is supported by the National Natural Science Foundation of China through the project NSFC 12222301, 12173007 and 11603002, the National Key Basic R&D Program of China via 2019YFA0405503 and Beijing Normal University grant No. 310232102. We acknowledge the science research grants from the China Manned Space Project with NO. CMS-CSST-2021-A08 and CMS-CSST-2021-A09. T.C.B. acknowledges partial support from grant PHY 14-30152, Physics Frontier Center/JINA Center for the Evolution of the Elements (JINA-CEE), and from OISE-1927130: The International Research Network for Nuclear Astrophysics (IReNA), awarded by the US National Science Foundation. His participation in this work was initiated by conversations that took place during a visit to China in 2019, supported by a PIFI Distinguished Scientist award from the Chinese Academy of Science.

This work has made use of data from the European Space Agency (ESA) mission Gaia (<https://www.cosmos.esa.int/gaia>), processed by the Gaia Data Processing and Analysis Consortium (DPAC, <https://www.cosmos.esa.int/web/gaia/dpac/consortium>). Funding for the DPAC has been provided by national institutions, in particular, the institutions participating in the Gaia Multilateral Agreement. Guoshoujing Telescope (the Large Sky Area Multi-Object Fiber Spectroscopic Telescope LAMOST) is a National Major Scientific Project built by the Chinese Academy of Sciences. Funding for the project has been provided by the National Development and Reform Commission. LAMOST is operated and managed by the National Astronomical Observatories, Chinese Academy of Sciences. We acknowledge the invaluable contribution of GALEX (NASA's Galaxy Evolution Explorer) in providing the dataset used in this research.

REFERENCES

- Abdurro'uf, Accetta, K., Aerts, C., et al. 2022, *ApJS*, 259, 35, doi: [10.3847/1538-4365/ac4414](https://doi.org/10.3847/1538-4365/ac4414)
- Ahumada, R., Allende Prieto, C., Almeida, A., et al. 2020, *ApJS*, 249, 3, doi: [10.3847/1538-4365/ab929e](https://doi.org/10.3847/1538-4365/ab929e)
- Alam, S., Albareti, F. D., Allende Prieto, C., et al. 2015, *ApJS*, 219, 12, doi: [10.1088/0067-0049/219/1/12](https://doi.org/10.1088/0067-0049/219/1/12)
- An, D., & Beers, T. C. 2020, *ApJ*, 897, 39, doi: [10.3847/1538-4357/ab8d39](https://doi.org/10.3847/1538-4357/ab8d39)
- Bailer-Jones, C. A. L., Rybizki, J., Fouesneau, M., Demleitner, M., & Andrae, R. 2021, *AJ*, 161, 147, doi: [10.3847/1538-3881/abd806](https://doi.org/10.3847/1538-3881/abd806)
- Beers, T. C., & Christlieb, N. 2005, *ARA&A*, 43, 531, doi: [10.1146/annurev.astro.42.053102.134057](https://doi.org/10.1146/annurev.astro.42.053102.134057)
- Bianchi, L., Conti, A., & Shiao, B. 2014, *VizieR Online Data Catalog*, II/335
- Brown, A. G. A., Vallenari, A., Prusti, T., et al. 2021, *Astronomy & Astrophysics*, 650, C3, doi: [10.1051/0004-6361/202039657e](https://doi.org/10.1051/0004-6361/202039657e)
- Buder, S., Asplund, M., Duong, L., et al. 2018, *Monthly Notices of the Royal Astronomical Society*, 478, 4513, doi: [10.1093/mnras/sty1281](https://doi.org/10.1093/mnras/sty1281)
- Buder, S., Sharma, S., Kos, J., et al. 2021, *Monthly Notices of the Royal Astronomical Society*, 506, 150, doi: [10.1093/mnras/stab1242](https://doi.org/10.1093/mnras/stab1242)
- Casagrande, L., Wolf, C., Mackey, A. D., et al. 2019, *MNRAS*, 482, 2770, doi: [10.1093/mnras/sty2878](https://doi.org/10.1093/mnras/sty2878)
- Deng, L.-C., Newberg, H. J., Liu, C., et al. 2012, *Research in Astronomy and Astrophysics*, 12, 735, doi: [10.1088/1674-4527/12/7/003](https://doi.org/10.1088/1674-4527/12/7/003)
- Fan, Z., Zhao, G., Wang, W., et al. 2023, *ApJS*, 268, 9, doi: [10.3847/1538-4365/ace04a](https://doi.org/10.3847/1538-4365/ace04a)
- Hong, J., Beers, T. C., Lee, Y. S., et al. 2023, *arXiv e-prints*, arXiv:2311.02297, <https://arxiv.org/abs/2311.02297>
- Huang, Y., Chen, B. Q., Yuan, H. B., et al. 2019, *ApJS*, 243, 7, doi: [10.3847/1538-4365/ab1f72](https://doi.org/10.3847/1538-4365/ab1f72)
- Huang, Y., Beers, T. C., Wolf, C., et al. 2021, *arXiv e-prints*, arXiv:2104.14154, <https://arxiv.org/abs/2104.14154>
- . 2022, *ApJ*, 925, 164, doi: [10.3847/1538-4357/ac21cb](https://doi.org/10.3847/1538-4357/ac21cb)
- Huang, Y., Beers, T. C., Yuan, H.-B., et al. 2023, *arXiv e-prints*, arXiv:2307.04469, doi: [10.48550/arXiv.2307.04469](https://doi.org/10.48550/arXiv.2307.04469)
- Ivezić, Ž., Sesar, B., Jurić, M., et al. 2008, *ApJ*, 684, 287, doi: [10.1086/589678](https://doi.org/10.1086/589678)
- Katz, D., Sartoretti, P., Guerrier, A., et al. 2023, *A&A*, 674, A5, doi: [10.1051/0004-6361/202244220](https://doi.org/10.1051/0004-6361/202244220)
- Li, H., Tan, K., & Zhao, G. 2018, *The Astrophysical Journal Supplement Series*, 238, 16, doi: [10.3847/1538-4365/aada4a](https://doi.org/10.3847/1538-4365/aada4a)
- Li, H., Aoki, W., Matsuno, T., et al. 2022, *The Astrophysical Journal*, 931, 147, doi: [10.3847/1538-4357/ac6514](https://doi.org/10.3847/1538-4357/ac6514)
- Lindgren, L., Bastian, U., Biermann, M., et al. 2021, *A&A*, 649, A4, doi: [10.1051/0004-6361/202039653](https://doi.org/10.1051/0004-6361/202039653)
- Liu, X. W., Yuan, H. B., Huo, Z. Y., et al. 2014, in *Setting the scene for Gaia and LAMOST*, ed. S. Feltzing, G. Zhao, N. A. Walton, & P. Whitelock, Vol. 298, 310–321, doi: [10.1017/S1743921313006510](https://doi.org/10.1017/S1743921313006510)
- Luo, A. L., Zhao, Y.-H., Zhao, G., et al. 2015, *Research in Astronomy and Astrophysics*, 15, 1095, doi: [10.1088/1674-4527/15/8/002](https://doi.org/10.1088/1674-4527/15/8/002)
- Majewski, S. R., Schiavon, R. P., Frinchaboy, P. M., et al. 2017, *AJ*, 154, 94, doi: [10.3847/1538-3881/aa784d](https://doi.org/10.3847/1538-3881/aa784d)
- Martin, D. C., Fanson, J., Schiminovich, D., et al. 2005, *ApJL*, 619, L1, doi: [10.1086/426387](https://doi.org/10.1086/426387)
- Martin, N. F., Starkenburg, E., Yuan, Z., et al. 2023, *arXiv e-prints*, arXiv:2308.01344, doi: [10.48550/arXiv.2308.01344](https://doi.org/10.48550/arXiv.2308.01344)
- Matteucci, F. 2021, *A&A Rv*, 29, 5, doi: [10.1007/s00159-021-00133-8](https://doi.org/10.1007/s00159-021-00133-8)
- Morrissey, P., Conrow, T., Barlow, T. A., et al. 2007, *The Astrophysical Journal Supplement Series*, 173, 682, doi: [10.1086/520512](https://doi.org/10.1086/520512)
- Morrissey, P., Conrow, T., Barlow, T. A., et al. 2007, *ApJS*, 173, 682, doi: [10.1086/520512](https://doi.org/10.1086/520512)
- Onken, C. A., Wolf, C., Bessell, M. S., et al. 2019, *PASA*, 36, e033, doi: [10.1017/pasa.2019.27](https://doi.org/10.1017/pasa.2019.27)
- Placco, V. M., Almeida-Fernandes, F., Arentsen, A., et al. 2022, *The Astrophysical Journal Supplement Series*, 262, 8, doi: [10.3847/1538-4365/ac7ab0](https://doi.org/10.3847/1538-4365/ac7ab0)
- Rockosi, C. M., Lee, Y. S., Morrison, H. L., et al. 2022, *ApJS*, 259, 60, doi: [10.3847/1538-4365/ac5323](https://doi.org/10.3847/1538-4365/ac5323)
- Schlegel, D. J., Finkbeiner, D. P., & Davis, M. 1998, *ApJ*, 500, 525, doi: [10.1086/305772](https://doi.org/10.1086/305772)
- Schwarzschild, M., Searle, L., & Howard, R. 1955, *ApJ*, 122, 353, doi: [10.1086/146094](https://doi.org/10.1086/146094)
- Soubiran, C., Le Campion, J.-F., Brouillet, N., & Chemin, L. 2016, *A&A*, 591, A118, doi: [10.1051/0004-6361/201628497](https://doi.org/10.1051/0004-6361/201628497)
- Soubiran, C., Le Campion, J. F., Cayrel de Strobel, G., & Caillo, A. 2010, *A&A*, 515, A111, doi: [10.1051/0004-6361/201014247](https://doi.org/10.1051/0004-6361/201014247)
- Starkenburg, E., Martin, N., Youakim, K., et al. 2017, *MNRAS*, 471, 2587, doi: [10.1093/mnras/stx1068](https://doi.org/10.1093/mnras/stx1068)

- Steinmetz, M., Zwitter, T., Siebert, A., et al. 2006, *AJ*, 132, 1645, doi: [10.1086/506564](https://doi.org/10.1086/506564)
- Suda, T., Yamada, S., Katsuta, Y., et al. 2011, *MNRAS*, 412, 843, doi: [10.1111/j.1365-2966.2011.17943.x](https://doi.org/10.1111/j.1365-2966.2011.17943.x)
- Suda, T., Katsuta, Y., Yamada, S., et al. 2008, *PASJ*, 60, 1159, doi: [10.1093/pasj/60.5.1159](https://doi.org/10.1093/pasj/60.5.1159)
- Suda, T., Hidaka, J., Aoki, W., et al. 2017, *PASJ*, 69, 76, doi: [10.1093/pasj/psx059](https://doi.org/10.1093/pasj/psx059)
- Wang, C., Huang, Y., Yuan, H., et al. 2022, *The Astrophysical Journal Supplement Series*, 259, 51, doi: [10.3847/1538-4365/ac4df7](https://doi.org/10.3847/1538-4365/ac4df7)
- Whitten, D. D., Placco, V. M., Beers, T. C., et al. 2021, *ApJ*, 912, 147, doi: [10.3847/1538-4357/abee7e](https://doi.org/10.3847/1538-4357/abee7e)
- Xu, S., Yuan, H., Niu, Z., et al. 2022a, *ApJS*, 258, 44, doi: [10.3847/1538-4365/ac3df6](https://doi.org/10.3847/1538-4365/ac3df6)
- Xu, S., Yuan, H., Zhang, R., et al. 2022b, *ApJS*, 263, 29, doi: [10.3847/1538-4365/ac9908](https://doi.org/10.3847/1538-4365/ac9908)
- Yamada, S., Suda, T., Komiya, Y., Aoki, W., & Fujimoto, M. Y. 2013, *MNRAS*, 436, 1362, doi: [10.1093/mnras/stt1652](https://doi.org/10.1093/mnras/stt1652)
- Yang, L., Yuan, H., Xiang, M., et al. 2022, *A&A*, 659, A181, doi: [10.1051/0004-6361/202142724](https://doi.org/10.1051/0004-6361/202142724)
- Yanny, B., Rockosi, C., Newberg, H. J., et al. 2009, *AJ*, 137, 4377, doi: [10.1088/0004-6256/137/5/4377](https://doi.org/10.1088/0004-6256/137/5/4377)
- Yoon, J., Beers, T. C., Placco, V. M., et al. 2016, *The Astrophysical Journal*, 833, 20, doi: [10.3847/0004-637X/833/1/20](https://doi.org/10.3847/0004-637X/833/1/20)
- York, D. G., Adelman, J., John E. Anderson, J., et al. 2000, *The Astronomical Journal*, 120, 1579, doi: [10.1086/301513](https://doi.org/10.1086/301513)
- Yuan, H., Liu, X., Xiang, M., Huang, Y., & Chen, B. 2015a, *ApJ*, 799, 134, doi: [10.1088/0004-637X/799/2/134](https://doi.org/10.1088/0004-637X/799/2/134)
- . 2015b, *ApJ*, 803, 13, doi: [10.1088/0004-637X/803/1/13](https://doi.org/10.1088/0004-637X/803/1/13)
- Yuan, H., Liu, X., Xiang, M., et al. 2015c, *ApJ*, 799, 133, doi: [10.1088/0004-637X/799/2/133](https://doi.org/10.1088/0004-637X/799/2/133)
- Zepeda, J., Beers, T. C., Placco, V. M., et al. 2023, *The Astrophysical Journal*, 947, 23, doi: [10.3847/1538-4357/acbbcc](https://doi.org/10.3847/1538-4357/acbbcc)
- Zhan, H. 2011, *Scientia Sinica Physica, Mechanica & Astronomica*, 41, 1441, doi: [10.1360/132011-961](https://doi.org/10.1360/132011-961)
- Zhang, R., & Yuan, H. 2023, *ApJS*, 264, 14, doi: [10.3847/1538-4365/ac9dfa](https://doi.org/10.3847/1538-4365/ac9dfa)
- Zhang, R.-Y., Yuan, H.-B., Liu, X.-W., et al. 2021, *Research in Astronomy and Astrophysics*, 21, 319, doi: [10.1088/1674-4527/21/12/319](https://doi.org/10.1088/1674-4527/21/12/319)

APPENDIX

A. MOTIVATION AND IMPACT OF ABSOLUTE MAGNITUDE

In our initial work, we used the relationship between stellar loci (NUV–BP and BP–RP colors) and metallicity to establish a model for estimation of photometric metallicities, as shown in Figure A1. The residuals $\Delta[\text{Fe}/\text{H}]_{\text{old}}$ in Figure A2 is calculated from this initial model as $[\text{Fe}/\text{H}]_{\text{GALEX}_{\text{old}}} - [\text{Fe}/\text{H}]_{\text{HR}}$. This relationship is represented by the colored lines in this figure. Apparently, $\Delta[\text{Fe}/\text{H}]_{\text{old}}$ exhibits some correlation with M_G , which means that M_G has an effect on our photometric metallicities, and a incorporation of M_G is essential. Consequently, we refine our model by factoring in the impact of M_G and indeed obtain better results than before.

The $\Delta[\text{Fe}/\text{H}]_{\text{old}}$ in the middle column of panels of Figure A3 is also calculated from our initial model as $[\text{Fe}/\text{H}]_{\text{GALEX}_{\text{old}}} - [\text{Fe}/\text{H}]_{\text{LAMOST}}$. Figure A3, which shows the comparison with LAMOST DR8, is an effective illustration of the difference (depicted by $\Delta[\text{Fe}/\text{H}]$) between the photometric metallicities and LAMOST metallicities. In the middle column of panels in Figure A3, we observe a distinct pattern in the distribution of $\Delta[\text{Fe}/\text{H}]_{\text{old}}$ with respect to M_G . As M_G increases, $\Delta[\text{Fe}/\text{H}]_{\text{old}}$ shows a structured variation, especially among metal-poor giants.

Based on these observations, we decided to incorporate absolute magnitude (M_G) into our model. The residuals $\Delta[\text{Fe}/\text{H}]_{\text{new}}$ in the right column of panels of Figure A3 is calculated from our new model as $[\text{Fe}/\text{H}]_{\text{GALEX}_{\text{new}}} - [\text{Fe}/\text{H}]_{\text{LAMOST}}$. This diagram demonstrates the changes in $\Delta[\text{Fe}/\text{H}]_{\text{new}}$ on the color-magnitude diagram, with black contours representing star density. We could consider the $\Delta[\text{Fe}/\text{H}]$ values of the majority of stars as being close to 0, indicating that our model is well-suited for the majority of giants. Furthermore, it is evident that the previously observed variation pattern is much weaker after considering M_G in our new model. Additionally, the typical deviations from $\Delta[\text{Fe}/\text{H}] = 0$ have been reduced, as indicated by the legends in each panel. However, there are a minority of $\Delta[\text{Fe}/\text{H}]$ values that display deviations from zero among the bluer BP – RP colors, shown in the shaded region in the bottom-middle panel. These stars could be interpreted as blue horizontal-branch stars and stars situated near the boundary between dwarfs and giants. Their properties slightly differ from those of most FGK giants in our sample. In any case, as illustrated here, this new version performs better compared with the old test result, successfully resolving the previously discernible trends related to M_G .

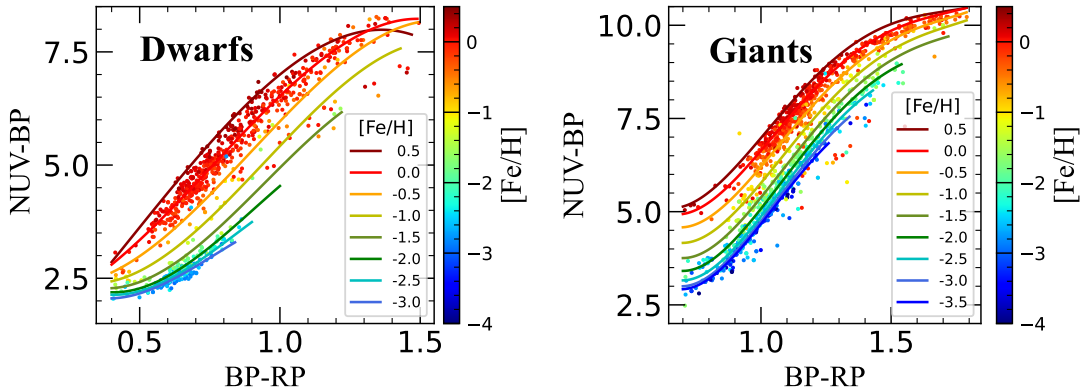


Figure A1. Distribution of the training sample in the (NUV – BP) vs. (BP – RP) plane, color-coded by $[\text{Fe}/\text{H}]$, with dwarfs in the left panel and giants in the right panel. The colored lines represent different $[\text{Fe}/\text{H}]$ values, ranging from +0.5 to –3.5 in steps of 0.5 dex.

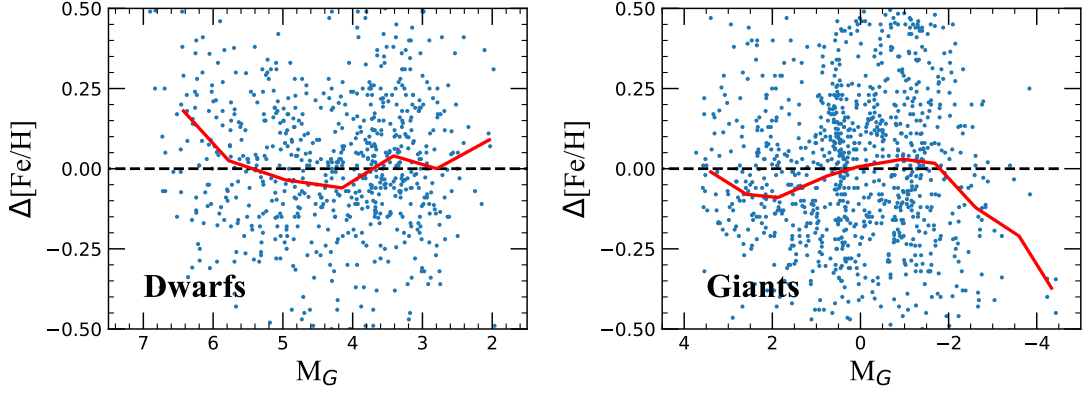


Figure A2. Distribution of the $\Delta[\text{Fe}/\text{H}]$ (calculated from the model without M_G) as a function of M_G for dwarf (left) and giant (right) stars, respectively. The red-solid line indicates the median values.

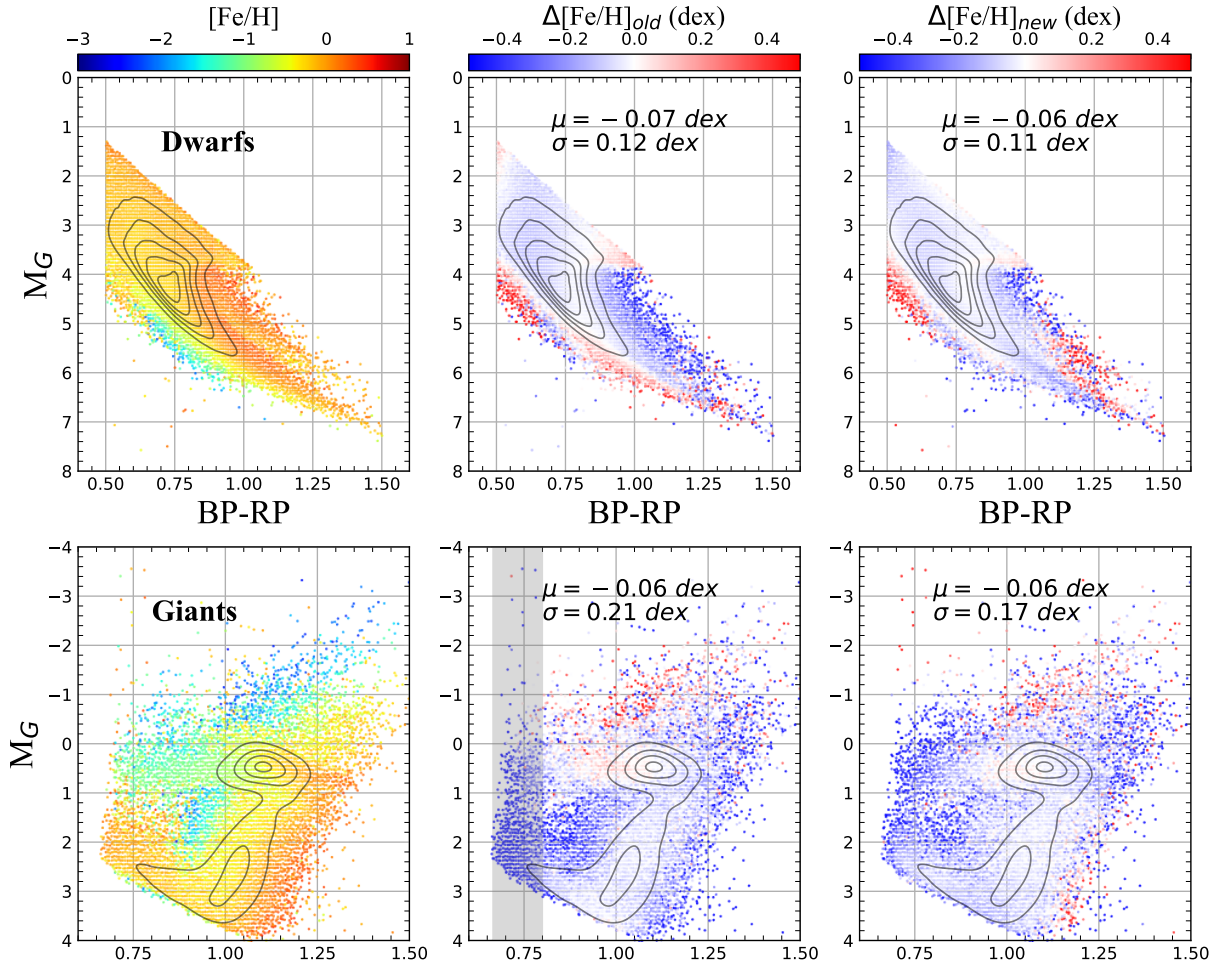


Figure A3. Color-magnitude diagram of the LAMOST DR8 test sample. Dwarfs are shown in the upper row of panels and giants are shown in the lower row of panels. The plots are color-coded by $[\text{Fe}/\text{H}]_{\text{LAMOST}}$ (left column of panels), $\Delta[\text{Fe}/\text{H}]$ (old model without M_G) (middle column of panels), and $\Delta[\text{Fe}/\text{H}]$ (new model with M_G considered) (right column of panels). In the lower middle panel, the shaded region indicates possible blue horizontal-branch stars or stars situated near the boundary between dwarfs and giants.